VOLUME 4 NUMBER 1 2017 ISSN 2409-6121

Physical Sciences and Technology

National Nano Laboratory of Open Type
Research Institute of Experimental and Theoretical Physics

Physical Sciences and Technology is publishing two number in a year by al-Farabi Kazakh National University, al-Farabi ave., 71, 050040, Almaty, the Republic of Kazakhstan
website: http://phst.kaznu.kz/

Any inquiry for subscriptions should be send to:
Abdiadil Askaruly, al-Farabi Kazakh National University
al-Farabi ave., 71, 050040, Almaty, the Republic of Kazakhstan
e-mail: Abdiadil.Askaruly@kaznu.kz

SCOPE AND AIM

Physical Sciences and Technology provides an original paperback for the publication of peer-reviewed research and review articles in all fields of Physics and related Technology. The topics, included in the scope, especially emphasize understanding of the physics underlying modern technology.

Subject areas may include, but are not limited to the following fields: Astronomy and Space Research, Theoretical Physics and Astrophysics, Plasma Physics and Related Technology, Chemical Physics and Radio Physics, Condensed Matter Physics and Related Technology, Thermal physics and Related Technology, Nuclear Physics and Related Technology, Nanomaterials and Nanotechnology, Applied Atomic and Molecular Physics, Material Sciences and Related Technology, Electronics and Related Technology, Instrumentation, Photonics and Quantum Electronics, Signal processing.

The Journal is issued under the auspices of the National Nano Laboratory of Open Type and the Research Institute of Experimental and Theoretical Physics and is published two times a year by the "Kazakh University" Publishing House. The International Editorial Board of the Journal consists of leading researchers from different countries of the world. The Journal is wide open for contributions that both lie at the far frontiers of contemporary physics and are particularly aimed at applications of the scientific principles of physics to modern technological problems.

UDC 539

Ion drift in parent gas for cesium, rubidium, and mercury

Golyatina R.I.*, Maiorov S.A.

Prokhorov General Physics Institute of the Russian Academy of Sciences, 38 Vavilov str., Moscow, 119991, Russia
**e-mail: mayorov_sa@mail.ru*

The results of Monte Carlo calculations of the ion drift characteristics in a constant and homogeneous electric field are presented for the values of the applied intensity in the range 1 <E / N <1000 Td for cesium, rubidium and mercury. The drift velocity, mean kinetic energy, longitudinal and transverse diffusion coefficients, mean free path, and the fraction of collisions with backward scattering are calculated.

PACS number(s): 51.50.+v,51.10.+y,52.80.Dy,52.25.Fi
Key words: ion, parent gas, vapor, drift, collision, hard-sphere model, cross-section, BGK model.

Introduction

The flow of ions in a constant homogeneous electric field is usually characterized by the drift velocity, the values of the average energies of ions, with coefficients of mobility and diffusion in the longitudinal and transverse directions. The velocity of the ion drift in a gas under the action of a constant homogeneous electric field is given by the relation

$$W = \mu E, \qquad (1)$$

where the coefficient of ion mobility $\mu(E,N,T)$ generally depends on both the field strength and gas parameters (temperature T, pressure $p = NT$, composition). A large number of experimental studies have been devoted to the determination of the diffusion coefficients and the mobility of ions in gases, and it can be assumed that in weak and moderately strong fields ($E/N < 1000\,Td$) the ion mobility is known with a very high accuracy <1% [1-4].

In the handbooks, experimental and calculated data are usually presented only the drift velocity, but other kinetic characteristics of the ion drift are necessary for analyzing the properties of the gas discharge. For example, to determine the ion Debye radius, it is necessary to know the average ion energy, taking into account their heating in an electric field. Many characteristics of a gas discharge are determined from the ionic distribution of velocities, and knowledge of the ion velocity distribution function is often sufficient.

In [5], a modeling technique used to calculate the ion drift characteristics in a gas is described. The results of calculations of the characteristics of ion drift in a constant and homogeneous electric field at 1<E/N<1000 for all noble gases. In this paper, which is a continuation of [6, 7], the results of molecular dynamics calculations are presented together with the Monte Carlo procedure for collision simulation. The characteristics of ion drift in a constant and homogeneous electric field at 1<E/N<1000 Td for cesium, rubidium and mercury are calculated.

In Table. 1 - 3 shows the flow characteristics of singly charged rubidium, cesium and mercury ions during their drift in a constant and homogeneous electric field in their own gas at atom temperature 300 K and atomic density 2.69 $*10^{19}$ $см^{-3}$. In addition to the drift velocity, the tables show: the effective temperature of the ions, which is related to the average kinetic energy of the ions by the ratio $\langle\varepsilon\rangle = \frac{1}{2}m\langle v^2\rangle = \frac{3}{2}T_{eff}$; temperature of ions along the field $T_{\|}$ and across the field $T_{\perp}$, so the average energy of the ion is equal to $\langle\varepsilon\rangle = \frac{1}{2}mW^2 + \frac{1}{2}T_{\|} + T_{\perp}$; the diffusion coefficients in the direction along and across the field, the mean free path, and the fraction of collisions with backward scattering with respect to the total number of collisions. The exact values of the various characteristics at intermediate points can be obtained by interpolation.

Table 1 – Characteristics of the cesium ion flow during their drift in a constant and homogeneous electric field in their own gas at 300 K and atomic density 2.69 10^{19}/cm^3.

E/N, Td	W, km/s	T_{eff}, K	$T_{\parallel}$, K	$T_{\perp}$, K	D_l cm^2/s	D_t cm^2/s	m.f.p. нм	BS / (BS+Iso)
1	0.0006	300.2	300.3	300.2	0.0056	0.0056	3.8	0.093
2	0.0012	300.2	300.3	300.2	0.0056	0.0056	3.8	0.093
5	0.0031	300.3	300.4	300.2	0.0056	0.0056	3.8	0.093
10	0.0062	300.4	300.7	300.3	0.0056	0.0056	3.8	0.093
20	0.0124	301.1	302.3	300.5	0.0056	0.0056	3.8	0.094
50	0.0310	306.1	313.7	302.2	0.0056	0.0056	3.8	0.095
100	0.0613	323.1	353.4	308.0	0.0057	0.0056	3.9	0.098
200	0.119	384.3	496.7	328.0	0.0060	0.0058	4.2	0.11
500	0.259	676.7	1199	415.3	0.0068	0.0063	5.4	0.16
1000	0.431	1259	2649	563.8	0.0078	0.0068	6.9	0.24

Table 2 – Characteristics of the rubidium ion flow during their drift in a constant and homogeneous electric field in their own gas at 300 K and the density of atoms 2.69 10^{19}/cm^3.

E/N, Td	W, km/s	T_{eff}, K	$T_{\parallel}$, K	$T_{\perp}$, K	D_l cm^2/s	D_t cm^2/s	m.f.p. nm	BS / (BS+Iso)
1	0.00041	300.2	300.4	300.2	0.0038	0.0038	3.3	0.11
2	0.00084	300.2	300.4	300.2	0.0038	0.0038	3.3	0.11
5	0.00212	300.2	300.4	300.2	0.0038	0.0038	3.3	0.11
10	0.0043	300.4	300.5	300.3	0.0038	0.0038	3.3	0.11
20	0.0085	300.9	301.7	300.5	0.0038	0.0038	3.3	0.11
50	0.0213	304.5	310.3	301.7	0.0039	0.0038	3.3	0.11
100	0.0423	317.2	340.0	305.8	0.0039	0.0038	3.4	0.12
200	0.0822	363.5	449.2	320.6	0.0040	0.0039	3.6	0.13
500	0.183	594.3	1006	388.5	0.0045	0.0042	4.5	0.17
1000	0.307	1070	2192	508.6	0.0051	0.0044	5.6	0.24

Table 3 – Characteristics of the mercury ion flow during their drift in a constant and homogeneous electric field in their own gas at 300 K and atomic density 2.69 10^{19}/cm^3.

E/N, Td	W, km/s	T_{eff}, K	$T_{\parallel}$, K	$T_{\perp}$, K	D_l cm^2/s	D_t cm^2/s	m.f.p. nm	BS / (BS+Iso)
1	0.0006	300.2	300.3	300.1	0.0055	0.0055	8.0	0.36
2	0.0012	300.2	300.3	300.1	0.0055	0.0055	8.0	0.36
5	0.0032	300.3	300.5	300.2	0.0055	0.0055	8.0	0.36
10	0.0063	300.7	301.5	300.3	0.0055	0.0055	8.0	0.36
20	0.0127	302.4	305.6	300.7	0.0055	0.0055	8.0	0.36
50	0.0313	313.4	333.5	303.3	0.0056	0.0055	8.2	0.37
100	0.061	348.4	422.7	311.3	0.0057	0.0055	8.6	0.38
200	0.113	457.8	704.6	334.4	0.0062	0.0054	9.6	0.41
500	0.243	969.3	2046	430.8	0.0099	0.0058	12.7	0.48
1000	0.441	2457	5937	716.4	0.0257	0.0085	18.3	0.53

The numerical data given above make it possible to obtain a fairly complete picture of the character of ion drift. We note some features of ion velocity distributions:

1) Analysis of the distribution functions shows that when ion drift, in conditions typical for gas-discharge plasma conditions, there is an appreciable heating of the ions not only in the longitudinal di-

rection, but also in the transverse direction. This is due to close collisions, when besides recharging, scattering also occurs at an arbitrary direction in the center-of-mass system;

2) Even at a sufficiently high reduced electric field strength an ion flow does not form supersonic flux, in which the velocity of thermal, chaotic motion would be less than the velocity of the directed motion - the drift velocity. As already noted, due to the fact that with increasing field strength simultaneously with the increase of drift velocity there is an increase in the dispersion of the distribution function of the ion velocity (i.e., the longitudinal and transverse temperatures);

3) In the velocity distribution of ions there is a large anisotropy (and a large difference between the longitudinal and transverse temperatures $T_{\parallel}$ and $T_{\perp}$). Therefore, the diffusion fluxes along and across the field can vary greatly in magnitude;

4) From the analysis of ion velocity distribution functions, from the analysis of other characteristics of the ion flux it follows that velocity module distribution, as well as the velocity projections, has significant differences from the corresponding Maxwellian distributions. Moreover, there is a difference not only in the tails of the distribution functions, but also in the central part. Accordingly, the distribution function of ion velocity during their drift in their own gas cannot be described by a Gaussian curve (shifted Maxwell distribution function).

In this connection, calculations were made with the determination of the fraction of collisions with backward scattering with respect to the total number of collisions, depending on the reduced field strength (naturally, the number of collisions does not include collisions with scattering at small angles due to divergence of the corresponding collision integral). The results of the calculations showed that there is an unexpected fact - although the cross sections with charge exchange are the largest, collisions with scattering back are only 15 - 45 percent. This takes place not only for the ions considered here for cesium, rubidium and mercury, but also for noble gases [7].

An analysis of the results of calculations shows that even in a strong field collisions with backward scattering are not dominant. But it is generally accepted that there is a decisive influence of collisions with the transfer of a charge, and often, when considering ion drift, only collisions with charge exchange are taken into account.

To take into account the effect of collisions on the velocity distribution of ions, the model collision integral of Bhatnagar, Gross, and Krook (integral BGK) is often used [6, 8-11]. However, the ion flow characteristics given in the calculations show a large deviation from the equilibrium distribution and a significant effect of collisions with isotropic scattering. In this connection, let us consider, as an example, the result of using BGK of the collision integral for analyzing the characteristics of the ion flux, taking into account only collisions with resonant charge exchange [7, 8].

The characteristics of the ion flux can be determined by solving the Boltzmann kinetic equation for the ion distribution function $f(\mathrm{v})$:

$$\frac{\partial f}{\partial t} + \mathrm{v}\nabla f + \frac{eE}{m}\frac{\partial f}{\partial \mathrm{v}} = I_{st}(f), \qquad (2)$$

where e – charge, m – ion mass, $I_{st}(f)$ – collision integral.

In a weakly ionized plasma, it is often possible to neglect elastic collisions of ions with atoms, electrons, and ions. Since in the case of collisions of ions with the atoms of the proper gas, the cross section for the resonant charge exchange of an ion is usually greatest, then we consider the kinetic equation (2) in the spatially homogeneous case with a constant electric field, taking into account only the resonant charge exchange of ions:

$$\frac{eE}{m}\frac{\partial f}{\partial u} = \int [f(\mathrm{v}')\varphi(\mathrm{v}) - f(\mathrm{v})\varphi(\mathrm{v}')]\left|\mathrm{v}-\mathrm{v}'\right|\sigma_{res} n_a d\,\mathrm{v}', \qquad (3)$$

where u - component of velocity along the direction of the electric field, σ_{res} - the cross section of resonant charge exchange, n_a - atomic density, The distribution functions of ions and atoms are normalized to unity: $\int f(\mathrm{v}) d\,\mathrm{v} = \int \varphi(\mathrm{v}) d\,\mathrm{v} = 1$. Equation (3) describes the process of ion transport, which is a relay character – this model was suggested by L. A. Sena [8, 12]. According to this model, the ion velocity after the collision is equal to the velocity of the atom with which it collided. This model does not take into account the change in the velocity of the atom during the collision.

Let us consider the model of ion motion in the case of the fulfillment of two conditions:

1) The drift velocity W considerably exceeds the thermal velocity of the atoms $W >> V_T = \left(T_i / m\right)^{1/2}$;

2) There are only collisions of one type-with a resonant charge exchange of ions on the atoms of the own gas.

When these conditions are met, we can neglect the thermal motion of the atoms and assume that the ions move uniformly accelerated in a constant electric field $E > 0$, stopping after each collision event. The condition $W >> V_T$ can be satisfied with good accuracy either in the case of a high electric field strength or at a low gas temperature.

In neglecting the thermal energy of the atoms and taking into account only collisions with charge exchange, the Boltzmann kinetic equation has the form [7, 8, 12]:

$$\frac{eE}{m}\frac{\partial f}{\partial u} = -f\frac{u}{\lambda_{st}},\ f(u<0)=0, \qquad (4)$$
$$f(0)=c_1 \quad .$$

If the cross section of resonant charge exchange depends on the velocity, then the ion distribution function has the form:

$$f(u) = c_1\Theta(u)\exp\left(-\frac{m}{eE}\int_0^u n_a\sigma_{res}(u')u'du'\right), \qquad (5)$$

where $\Theta(u)$ - Heaviside function, c_1 – the constant, determined from the normalization condition.

If the cross section of resonant charge exchange and the mean free path of the ion $\lambda_{st} = 1/\sigma_0 n_a$ do not depend on the velocity, then the solution of (4) has the form

$$f(u) = \Theta(u)\left(\frac{2m}{\pi T_E}\right)^{1/2}\exp\left(-\frac{mu^2}{2T_E}\right), \qquad (6)$$

where $T_E \equiv eE\lambda_{st}$. The distribution (6) is half the Maxwell distribution with a temperature equal to the energy recruited by the ion at the mean free path. Consequently, the average kinetic energy of the ions, due to the motion in the direction of the field, is $\frac{1}{2}m\langle u^2\rangle = \frac{1}{2}T_E = \frac{1}{2}eE\lambda_{st}$. The ion flux density for this distribution is $J_i = n_i\left(2eE\lambda_{st}/\pi m\right)^{1/2}$, the average ion velocity (drift velocity) is $W = \left(2eE\lambda_{st}/\pi m\right)^{1/2} = \left(2T_E/\pi m\right)^{1/2}$.

Collisions with charge exchange play the most important role, but collisions of other types have a significant effect on the characteristics of ion velocity distribution. In addition to collisions with recharging, an important role can be played by polarization and gas-kinetic collisions. In the case of such collisions, the ion does not stop, but dissipates at the fixed center in the center-of-mass system of the atom-ion. A good approximation of this type of collision is the model of hard spheres, i.e. isotropic scattering. Without consideration of these collisions, heating of the ions in the transverse direction can not be taken into account. By analogy with the hydrodynamic approximation, it is often assumed that the drift of ions in a strong field is described by the shifted distribution function of Maxwell:

$$f_0\left(\bar{v}\right) = \left(\frac{m}{2\pi T_i}\right)^{3/2}\exp\left(-\frac{m[(u-W)^2+v^2+w^2]}{2T_i}\right). \qquad (7)$$

This distribution has two parameters - the drift velocity W and the ion temperature T_i, which determines the thermal dispersion of the ion velocities $V_i = \left(T_i/m\right)^{1/2}$, here the direction of the field and drift coincides with the x axis.

To take into account the impact of collisions, the model collision integral of Bhatnagar, Gross, and Kruk (BGK integral) is often used [7-9]:

$$I_{st} = \frac{\varphi - f}{\tau_0}, \qquad (8)$$

which describes the relaxation of the ion distribution function f to the equilibrium distribution function of atoms φ with a characteristic relaxation time τ_0 = const. The BGK integral qualitatively correctly describes the process of plasma relaxation to equilibrium in the case of a slight deviation from it. But it is inapplicable if the collision frequency of ions with atoms depends on their relative velocity, or the deviation from equilibrium is large. The ion transport equation in the spatially homogeneous case has the form: $V_E\,\partial f/\partial u = \varphi(u) - f(u)$, where $V_E = eE\tau_0/m$. Its solution has the form:

$$f_E(u) = \frac{1}{V_E}\int_{-\infty}^{u}\varphi(u')\exp\left(-\frac{u-u'}{V_E}\right)du'. \qquad (9)$$

In the case of a subthermal flow velocity, when the drift velocity $W \le \left(T/m\right)^{1/2}$, and the Maxwellian distribution of atoms $\varphi(u) = (m/2\pi T_0)^{1/2}\exp\left(-mu^2/2T_0\right)$, the solution (2) with the collision integral (8) has the form

$$f(u) = \varphi(u)(1 + uV_E/V_T^2)\ . \qquad (10)$$

This distribution coincides with the expansion of the shifted Maxwellian distribution (7) at $V_E = W << V_T = (T/m)^{1/2}$. As expected, in the case of a small deviation from equilibrium, the use of the model integral BGK gives a reasonable result. In the case of a high ion flow rate $W >> V_T = \sqrt{T_0/m}$ and a Maxwellian distribution of atoms, the distribution (9) has the asymptotics:

$$f(u) = \frac{\Theta(u)}{V_E} \exp\left(-\frac{u}{V_E}\right). \qquad (11)$$

This distribution describes the uniformly accelerated motion of ions in a constant electric field $E > 0$, which stop after each collision event, the probability of which does not depend on the velocities of the ion and the atom. This unnatural hybrid model (taking the properties of polarization and resonant collisions) is a consequence of the structure of the integral BGK for large fields, when $W >> (T/m)^{1/2}$. It does not take into account the difference of the ion velocity from zero after the collision.

If we neglect the thermal motion of the atoms in comparison with the flow velocity and represent the distribution function of atoms in the form $\varphi(u) = \delta(u)$, then the particle profit in the BGK integral has the form $I^+_{BGK} = \varphi/\tau_0$, the decrease is $I^-_{BGK} = f/\tau_0$. For collisions with a resonant predissection at a constant cross section, the profit and loss of the particles has, respectively, a form $I^+_{res} = \varphi/\tau_0$, a decrease - $I^-_{res} = \sigma_0 n_a u f$. Consequently, the BGK integral even incorrectly conveys the nature of the particle loss at a qualitative level, this explains the radical difference between the distribution (11) and the physically reasonable distributions (6) and (7).

For polarization collisions characterized by a constant mean free path, the particle loss in the BGK integral can be reduced to the form $I^-_{pol} = f/\tau_0$. But the profit of particles in the collision integral depends on the entire distribution function and can in no way be approximated by the quantity $I^+_{BGK} = \varphi/\tau_0$. This means that, regardless of the form of the distribution function $f(\mathrm{v})$, the number of ions scattered as a result of collisions into a group with velocities v, is equal to the number of ions that would be scattered from this group in the case of an equilibrium distribution at a collision frequency independent of velocity [9].

The BGK integral does not allow to take into account the following factors:

1) for collisions characterized by a constant cross section (charge exchange, gas-kinetic), it does not take into account the dependence of the collision probability on the velocity;

2) for collisions characterized by a constant mean free path (polarization collisions), he does not take into account the difference between the ion velocity after the scattering event from zero.

These factors are decisive at a drift velocity comparable to the thermal velocity of the atoms. Consequently, the BGK integral is inapplicable for the problem of determining the characteristics of the ion drift in its own gas.

Let us compare the results of calculating the drift velocity of cesium, rubidium and mercury ions in the own gas with the drift velocity from the solution of the Boltzmann equation with the integral of the BGK collisions [7]:

$$\frac{W}{V_T} = \frac{F(F^{1/2}+1)}{\pi^{1/2}(1+F^{1/2}+F)}. \qquad (12)$$

In Figure 1 shows the results of calculating the drift velocity of an ion in its own gas, depending on the electric field strength for cesium, rubidium and mercury. In Figure 2 shows the same results, but the drift velocity is normalized to the value of the thermal velocity (the velocity of an ion with an energy equal to the temperature of the atoms), and the field is normalized by the value of the characteristic "heating field": $F = E/E_T$. The magnitude of the heating field is determined in such a way that an energy equal to the temperature of the atoms is accumulated on the mean free path.

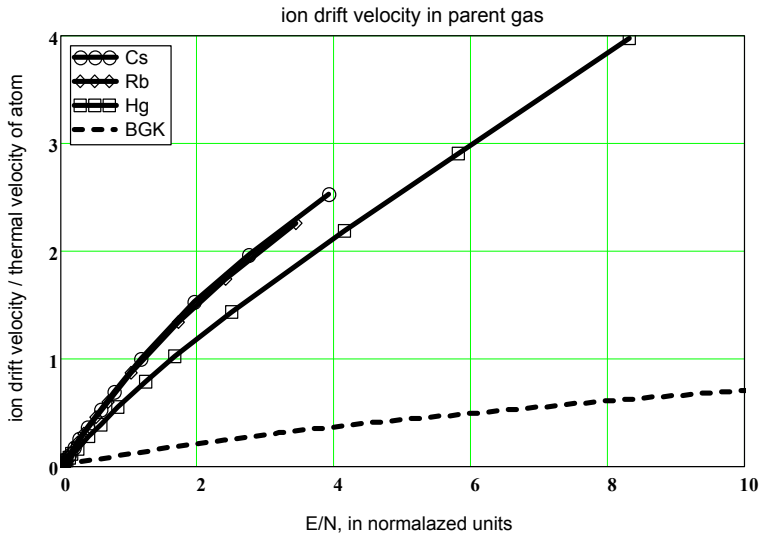

Figure 1 – Results of calculating the drift velocity of an ion in its own gas as a function of the electric field strength in dimensionless units. The drift velocity is normalized to the value of the thermal velocity (the velocity of an ion with an energy equal to the temperature of the atoms), the field is normalized to the value of the characteristic "heating field", in which an energy equal to the temperature of the atoms is accumulated on the mean free path. The shaded curve is the solution of the Boltzmann equation with the BGK collision integral (11).

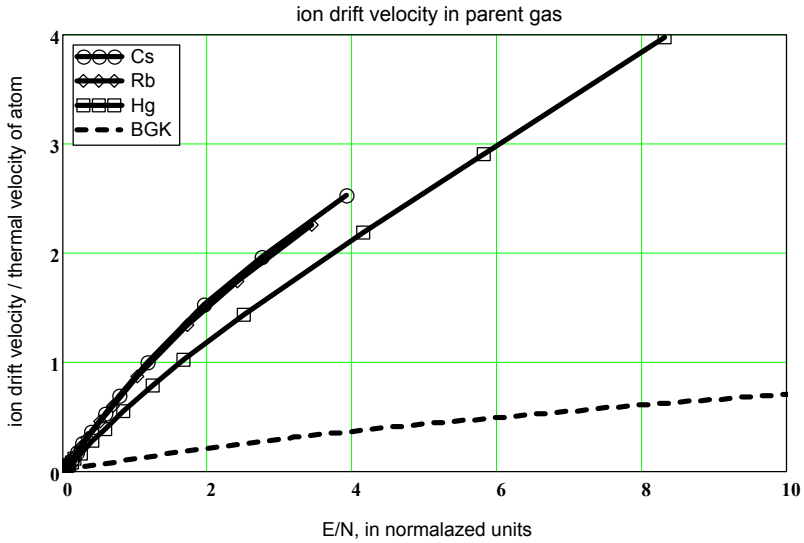

Figure 2 – Results of calculating the drift velocity of an ion in its own gas as a function of the electric field strength in dimensionless units. The drift velocity is normalized to the value of the thermal velocity (the velocity of an ion with an energy equal to the temperature of the atoms), the field is normalized to the value of the characteristic "heating field", in which an energy equal to the temperature of the atoms is accumulated on the mean free path. The shaded curve is the solution of the Boltzmann equation with the BGK collision integral (11)

Conslusion

The above graphs make the following conclusions:

1) The introduction of dimensionless units makes it possible to reduce the characteristics for different gases to universal curves;

2) The BGK collision integral for the problem of ion drift in an own gas leads to significant errors, which does not allow even describing real processes at a qualitative level (see, for example [7-9]);

3) There is an unexpected and nontrivial fact: although cross sections with charge exchange are the largest, collisions with backward scattering make up only 15-45 percent for noble gases at 300 K (for this reason see [16], where an attempt was made to approximate collisions in the form of a sum of collisions with isotropic scattering and backscattering).

The analysis showed that such a large difference in the calculations and the BGK theory is due to the fact that even in a strong field, collisions with backward scattering are not dominant. The results of the calculations demonstrate that the approach to the analysis of ion drift based on the BGK collision integral [10] is accompanied by large errors. These features of ion drift play an important role when considering the properties of cryogenic discharges and in a mixture of gases [5, 13-15]. The above numerical data explain the results of the analysis of ion-atom collisions [16] and significantly supplement the reference data [1-4].

References

1. E. W. McDaniel, E. A. Mason. The Mobility and Diffusion of Ions in Gases // Wiley. – New York. – P. 1973.

2. H.W. Ellis, R.Y. Pai, E.W. McDaniel, E.A. Mason, L.A.Viehland // Atomic Data and Nuclear Data Tables. – 1976. – Vol. 17. – No 3. – P. 177.

3. E.W. McDaniel, L.A.Viehland. The transport of slow ions in gases: Experiment, theory, and applications // Physics Reports. – 1984. – Vol. 110. No. 5–6. – P. 333.

4. E.A. Mason, L.A.Viehland // Atomic Data and Nuclear Data Tables. – 1995. – Vol. 60. – No. 1. – P. 37.

5. S.A. Maiorov. Ion drift in a gas in an external electric field // Plasma Phys. Rep. – 2009. – Vol. 35. – P. 802.

6. S. A. Maiorov, V. N. Tsytovich, B. Lebedev. On the accuracy of the BGK model for ion drift in own gas // Phys. Inst. – 2012. – Vol. 39. – P. 72.

7. R.I. Golyatina, S.A. Maiorov. Approximation of the characteristics of ion drift in parent gas // Plasma Physics Reports. – 2017. – Vol. 43. – No. 1. – P. 75.

8. B.M. Smirnov. // Physics of Ionized Gases. – Wiley–VCH. – 2001.

9. G.A. Bird. // Molecular gas dynamics. – Oxford University Press. – 1976.

10. D. Else, R. Kompaneets, S. V. Vladimirov. // Phys. Plasmas. – 2009. – Vol. 16. – P. 062106.

11. M. Lampe, T. B. Röcker, G. Joyce, S. K. Zhdanov, A. V. Ivlev, G. E. Morfill. Ion distrbution function in a plasma with uniform electric field // Phys. Plasmas. – 2012. – Vol. 19. – P. 113703.

12. L. A. Sena. Inelastic Collisions of Light Atoms in the Adiabatic Approximation // JETP. – 1946. – Vol. 16. – P. 734;

13. S.A. Maiorov, T.S. Ramazanov, K.N. Dzhumagulova, A.N. Jumabekov, A.N.Dosbolaev. Investigation of plasma–dust structures in He-Ar gas mixture // Phys. Plasm. – 2008. – Vol. 15. – P. 093701.

14. S. N. Antipov, E. I. Asinovskii, A. V. Kirillin, S. A. Maiorov, V. V. Markovets, O. F. Petrov, V. E. Fortov. Charge and Structures of Dust Particles in a Gas Discharge at Cryogenic Temperatures // JETP. – 2008. – Vol. 106. – P. 830.

15. S. N. Antipov, M. M. Vasil'ev, S. A. Maiorov. O. F. Petrov, V. E. Fortov. Dusty plasma structures in He–Kr DC glow discharge //JETP. – 2011. – Vol. 112. – P. 482.

16. D. Piscitelli, A.V. Phelps, J. Urquijo, E. Basurto, L.C. Pitchford. Ion mobilities in Xe/Ne and other rare-gas mixtures // Phys. Rev. E. – 2003. – Vol. 68. – P. 046408.

UDC 539.17

Whittaker asymptotics of shell-model wave functions for excited states of ^{13}C

[1*]Burkova N.A., [2]Afanasyeva N.V., [1]Sharafutdinova D.N.

Physical-Technical department, al-Farabi Kazakh National University, Almaty, Kazakhstan
[2]Institute of Nuclear Physics, Almaty, Kazakhstan
[*]e-mail: natali.burkova@gmail.com

Halo and skin structure of $1/2^+$, $3/2^+$, $5/2^+$ excited states of ^{13}C nucleus is under investigation. The modified radial functions have been constructed basing on the shell model functions. The matching procedure was performed while using the corresponding Whittaker exponential-like asymptotics. To find the matching radius via the oscillator parameter r_0 three options were examined related to the experimental and theoretical data on the mean square radii, and uncertainty relation. The renormalization of the modified functions shows the input of the asymptotic region near 15-20%. The most qualitative effect is the redistribution of the probability density both at short and long-range distances. The obtained functions are given as parametrization by Gauss basis.

Key words: halo nuclei, skin state, shell model, oscillator parameter, Whittaker function, matching radius.
PACS: 24.10

Introduction

Currently, vast experimental material is assembled on the study the unusual properties of some atomic nuclei, known as the halo-states [1-5]. The defining feature of a halo was from the beginning understood to be a large spatial extension caused by neutrons tunneling out from a nuclear core. Nuclei may reveal not only well-developed *halo* states but also something intermediate between normal nuclei and halo nuclei, so called *skin*-states.

Halo effect research attractiveness that is quite enough reliably identify two main features of halo states as large root mean radius r_{ms} and narrow localized impulse distributions. These two characteristics, obviously, related to each other according the Heisenberg uncertainty relation ($\Delta x \Delta p \sim \hbar$).

Despite the seeming simplicity and transparency of the question, both experimental and theoretical studies still face certain difficulties. First of all, it is ambiguity on rms radii data [6-7]. The difficulty lies in the fact that the lifetime of most neutron-rich isotopes is extremely short and is typically a few milliseconds. It is therefore to work with short-lived isotopes needed entirely new technique, compared with conventional ones.

Recent advances are related to the collinear laser beams and anti-collinear technologies (CACLB) of the European Organization for Nuclear Research. Today, the installation ISOLDE at CERN synthesized radioactive isotopes up to Z = 10 in a collision energy of 1.4 GeV protons on uranium carbide target. Currently, it reports on the results of measurements of the charge and mass and radii for ^{7,9,10}Be isotopes by laser spectroscopy [8]. With great precision, it was found that ^{11}Be is a halo-nucleus with a radius of 7 *fm*, to compare ^{10}Be isotope core radius is 2.5 *fm*. Experiments are planned to heavier isotopes, particularly for the carbon-oxygen group.

Theoretical models deal with the description of the nuclei with prominent α- cluster structure, which include the majority of *p*-shell nuclei, may be represented as a semi-phenomenological and microscopic. The first, are the cluster models and their various modifications [9]. To the second ones may refer the models such as the resonating group method (RGM), the method of K-harmonics, variational Monte Carlo (VMC), the method of fermion molecular dynamics (FMD), and others. It is believed that microscopic models not contain adjustable parameters. However, they are based on the nucleon-nucleon potentials, which, in turn, are fitted according to the elastic *NN* – scattering in a wide range of energies, so there are parameters a lot.

At the same time almost all the model approaches are based exactly on the data on the shell structure of atomic nuclei, as on the comparative, which are considered at the present time as the classic ones and obtained in the framework of the shell model (SM), which has only one oscillator parameter r_0.

For the halo-states the radial functions that characterize the distribution of the probability density, can be divided into *internal* and *external* conventional parts. The first is a model-depending, and the second asymptotic one is model-independent. The last one determines the mean square r_{ms} size of the nuclear system, as well as so-called asymptotic normalization coefficient (ANC), which can be measured experimentally [10-11]. All models somehow have to "converge" in the section point, call it a matching radius r_m of these two areas. Thus, this is the main task to identify and substantiate the value of the r_m radius.

Present paper reports on the modification of oscillatory wave functions for low-lying 2s-, 2d-excited states with $J^{\pi} = 1/2^{+}, 3/2^{+}, 5/2^{+}$ of ^{13}C nucleus. To construct the modified functions we have used the matching procedure of oscillatory wave functions with corresponding Whittaker functions.

In this context, the lower bound of the asymptotic region r_m is defined, and it allows to answer a question about a pronounced halo, skin- or normal structure of these states. The advantage of using the shell model is that almost all the calculations can be carried out analytically.

Modification procedure for the oscillator radial wave functions

We are basing on the fundamental postulate of nonrelativistic quantum mechanics telling that functions to be regarded as wave functions (WF) should be square integrated, continuous, unambiguous, and final.

Assume the potential in Schrodinger radial equation is defined in two space intervals $0 < r \le r_m$ and $r_m \le r < \infty$. Such a division is conventional, and depending on the properties of the treating microsystem may consist of more than two intervals. Let us restricted by one transition point.

The matching radius r_m we can find unambiguously from the continuity condition

$$\begin{cases} u_1(r_m) = u_2(r_m) & (a) \\ u_1'(r_m) = u_2'(r_m) & (b) \end{cases} \qquad (1)$$

Here $u_1(r)$ is any model function that should be modified providing the correct extended asymptotic behavior by some appropriate analytical $u_2(r)$ function. As $u_1(r)$ the shell model radial oscillator WF have been used $u_1(r)=R_{n\ell}(r)$ for the state with main quantum number n and orbital momentum ℓ. For $u_2(r)$ various functions with exponential asymptotic at $r \to \infty$ may be used. Here we are taking $W_{0,\ell}(z)$ Whittaker functions [12] as $u_2(r)$

$$u_2(r) = C_{n\ell} \frac{\sqrt{2k_0}}{r} W_{0,\ell}(z), \qquad (2)$$

where $z = 2k_0 r$ – dimensionless variable, k_0 – wave number. Factor $C_{n\ell}$ is asymptotic normalization coefficient.

To operate with functions of one and the same dimension expression (2) should be rewritten as the following

$$u_2(r) = C_{n\ell} \omega_{0,\ell}(r),$$

$$\omega_{0,\ell}(r) = \frac{\sqrt{2k_0}}{r} W_{0,\ell}(z). \qquad (3)$$

Therefore, the continuity condition (1) may be represented as equation of type

$$\frac{R_{n\ell}'(r)}{R_{n\ell}(r)} = \frac{\omega_{0,\ell}'(r)}{\omega_{0,\ell}(r)}, \qquad (4)$$

and the corresponding real roots define the matching radius r_m. The solutions may be found analytically or numerically. To find asymptotic constant $C_{n\ell}$ equation (1a) is used

$$C_{n\ell} = \frac{R_{n\ell}(r_m)}{\omega_{0,\ell}(r_m)}. \qquad (5)$$

Basing on the obtained values of r_m and $C_{n\ell}$, the modified radial channel functions are now defined as following

$$R_{n\ell}^{mod}(r) = \begin{cases} R_{n\ell}(r), & 0 < r \le r_m \\ C_{n\ell}\omega_{0,\ell}(r), & r_m \le r < \infty \end{cases} \qquad (6)$$

The modified functions $R_{n\ell}^{mod}(r)$ should be normalized on to unit according the standard procedure

$$N^2\int_0^{\infty}\left(R_{n\ell}^{\mathrm{mod}}\right)^2 r^2dr=1. \qquad (7)$$

This expression has the explicit form while taking definition (6) into account:

$$N^2\left[\int_0^{r_m}R_{n\ell}^2r^2dr+C_{n\ell}^2\int_{r_m}^{\infty}\omega_{0,\ell}^2r^2dr\right]=1. \qquad (8)$$

To continue our notations let us introduce I_1 and I_2 for the first and second integrals in (8) respectively, then the normalizing constant N is

$$N=\frac{1}{\sqrt{I_1+C_{n\ell}^2I_2}} \qquad (9)$$

Finally the normalized modified radial function is defined as $\tilde{R}_{n\ell}^{mod}(r)=N\cdot R_{n\ell}^{mod}(r)$, or taking into account (6) one arrives

$$\tilde{R}_{n\ell}^{mod}(r)=\begin{cases}N\cdot R_{n\ell}(r), & 0<r\le r_m\\ N\cdot C_{n\ell}\omega_{0,\ell}(r), & r_m\le r<\infty.\end{cases} \qquad (10)$$

It is formal to somewhat extent, but it makes obvious that all relations for obtaining of matching radius r_m and ANC $C_{n\ell}$ preserve.

To characterize the probability density in interior and exterior regions it is natural to introduce the corresponding weights

$$\begin{cases}P_{in}=N^2\cdot I_1, & 0<r\le r_m\\ P_{out}=N^2\cdot C_{n\ell}^2I_2, & r_m\le r<\infty,\end{cases} \qquad (11)$$

there relative probabilities P_{in} and P_{out} will be given in %.

For completeness let us present the analytical expression for the Whittaker functions (3) obtained for the special case of zero Coulomb potential

$$W_{0,l}(z)=e^{-z/2}\sum_{n=0}^{l}z^{-n}\frac{(l+n)!}{(l-n)!n!}. \qquad (12)$$

Modified functions in space representation

Here we are giving the results of the calculations for the modified radial WF of the low-lying excited states $J^{\pi}=1/2^+$, $3/2^+$ and $5/2^+$ of positive parity π with total momentum J in ^{13}C nucleus corresponding to the $s^4p^8(2\mathrm{s}-1\mathrm{d})^1$ configuration with ^{12}C as a core and a valence neutron in 2s-1d shell. The choice of these states is due to the fact that they are the real candidates for the manifestation of skin or halo structure on grounds such as large rms radii r_{ms}, small binding energy of the valence neutron $\varepsilon=\hbar^2k_0^2/2\mu$.

For the first excited state $J^{\pi}=1/2^+$ with excitation energy E_{exc}=3,089 MeV oscillator $R_{2s}(r)=\frac{\sqrt{6}}{\pi^{1/4}}\cdot\frac{1}{r_0^{3/2}}\left(1-\frac{2r^2}{3r_0^2}\right)e^{-\frac{r^2}{2r_0^2}}$ function was used. For the other $J^{\pi}=5/2^+$ and $3/2^+$ states with the excitation energies E_{exc}=3,854 and 7,67 MeV $R_{2d}(r)=\frac{4}{\pi^{1/4}\sqrt{15}}\cdot\frac{r^2}{r_0^{7/2}}e^{-\frac{r^2}{2r_0^2}}$ radial function was employed.

Let us define how the appropriate parameters necessary for the modification procedure may be determined.

Method №1 consider the parameter k_0 to be known from the relation $\varepsilon=\hbar^2k_0^2/2\mu$. Then using ρ_0 as the solution of equation (4) and relation $\rho_0=k_0r_m$, the matching radius r_m may be found. Finally the oscillator parameter we can obtain from $r_0=1/k_0$.

Method №2 for the definition of oscillator parameter is basing on the known correlation for the 3D harmonic oscillator $\overline{r^2}=r_0^2\cdot(n+3/2)$, using the rms value r_{ms} the oscillator parameter r_0 may be obtained. The matching radius r_m is coming from the relation $\rho_0=r_m/r_0$.

We obtained the numerical values: $\rho_0=2,474556$ for R_{2s} matching function as well as $\rho_0=2,513260$ in case of R_{2d}. Table 1 is a summary of all obtained parameters with pointed above method in last column.

Table 1 – Parameters of excited states $J^{\pi}=1/2^+$, $5/2^+$, $3/2^+$ of ^{13}C

J^{π}	E_{exc}, MeV	r_{rms}, *fm*	r_m, *fm*	r_0, *fm*	**№**
$1/2^+$	3,089	$5,04\pm0,75$	6,669	2,695	***2***
			8,604	3,477	***1***
$5/2^+$	3,874	$3,68\pm0,4$	4,946	1,968	***2***
			11,393	4,533	***1***
$3/2^+$	7,67	-	7,218	2,872	***1***

The resulting modified functions in space representation have been expanded by Gaussian basis. In case of $J^{\pi} = 1/2^{+}$ state the expansion coefficients are given in table 2 for the corresponding function of the form

$$\tilde{R}_{2s}^{mod}(r) = \sum_{i=1}^{15} B_i \cdot e^{-\beta_i \vec{r}^2} \quad . \qquad (13)$$

In case of $J^{\pi} = 5/2^{+}$ and $3/2^{+}$ states the corresponding expanded function is of the form

$$\tilde{R}_{2d}^{mod}(r) = r^2 \sum_{i=1}^{15} D_i \cdot e^{-\gamma_i \vec{r}^2} \quad . \qquad (14)$$

Corresponding expansion coefficients are given in tables 3 and 4.

Table 2 – Expansion coefficients for $1/2^{+}$ excited state of ^{13}C corresponding data of Table 1

i	**№ 2** β_i	B_i	**№1** β_i	B_i
1	0.995675768D-02	-0.214390442D-01	0.779153573D-02	-0.157705075D-01
2	0.336098351D-01	-0.189661409D+00	0.263009545D-01	-0.320160296D+00
3	0.599294538D-01	-0.190958104D+00	0.468970417D-01	0.188133220D+01
4	0.889974970D-01	0.464299511D+01	0.696438740D-01	-0.142428669D+02
5	0.121524851D+00	-0.323408024D+02	0.950977468D-01	0.577866466D+02
6	0.158690793D+00	0.104349783D+03	0.124181488D+00	-0.133732675D+03
7	0.202296685D+00	-0.185342008D+03	0.158304731D+00	0.201189391D+03
8	0.255142402D+00	0.204894845D+03	0.199658483D+00	-0.205576264D+03
9	0.321792941D+00	-0.147094874D+03	0.251815026D+00	0.144536068D+03
10	0.410216901D+00	0.688772842D+02	0.321010086D+00	-0.694744674D+02
11	0.535673529D+00	-0.205394784D+02	0.419184595D+00	0.222793718D+02
12	0.731454805D+00	0.368965561D+01	0.572390775D+00	-0.454905888D+01
13	0.108623797D+01	-0.359689964D+00	0.850021890D+00	0.545615092D+00
14	0.193686319D+01	0.155681470D-01	0.151566798D+01	-0.333966034D-01
15	0.653803936D+01	-0.195974076D-03	0.511626062D+01	0.835301964D-03

Table 3 – Expansion coefficients for $5/2^{+}$ excited state of ^{13}C corresponding data of Table 1

i	**№2** γ_i	D_i	**№1** γ_i	D_i
1	0.934423119D-02	0.193301166D-04	0.507316101D-02	0.153278531D-04
2	0.282397165D-01	0.102243489D-02	0.171248624D-01	0.107571441D-02
3	0.477749532D-01	-0.839234710D-02	0.305352182D-01	-0.293365722D-02
4	0.684424019D-01	0.899360796D-01	0.453459496D-01	0.570832256D-01
5	0.908476504D-01	-0.425774826D+00	0.619192670D-01	-0.242640999D+00
6	0.115788434D+00	0.118540758D+01	0.808560348D-01	0.616231656D+00
7	0.144383322D+00	-0.156836386D+01	0.103074082D+00	-0.103888477D+01
8	0.178298554D+00	-0.991321547D-01	0.129999999D+00	0.120998646D+01
9	0.220180378D+00	0.411323404D+01	0.163959740D+00	-0.988919594D+00
10	0.274555699D+00	-0.670385983D+01	0.209013461D+00	0.567618348D+00
11	0.349930621D+00	0.537336858D+01	0.272936045D+00	-0.226320361D+00
12	0.464483627D+00	-0.243539615D+01	0.372690399D+00	0.613817482D-01
13	0.665419299D+00	0.632727569D+00	0.553459300D+00	-0.110395726D-01
14	0.112573289D+01	-0.935347961D-01	0.986869335D+00	0.132846869D-02
15	0.340214046D+01	0.112954444D-01	0.333125777D+01	-0.177390635D-03

Table 4 –Expansion coefficients for $3/2^+$ excited state of ^{13}C corresponding data of Table 1

i	**№1** γ_i	D_i	i	γ_i	D_i
1	0.585738861D-02	0.118469219D-05	9	0.189305230D+00	0.107028918D+01
2	0.197720856D-01	0.309624471D-03	10	0.241323519D+00	-0.114006343D+01
3	0.352554628D-01	-0.523338692D-03	11	0.315127487D+00	0.713878510D+00
4	0.523556906D-01	0.195186077D-01	12	0.430302230D+00	-0.278365868D+00
5	0.714909714D-01	-0.737727901D-01	13	0.639015042D+00	0.682627507D-01
6	0.933550533D-01	0.212603276D+00	14	0.113942317D+01	-0.108208117D-01
7	0.119007646D+00	-0.110494484D+00	15	0.384621565D+01	0.184247221D-02
8	0.150095869D+00	-0.452967220D+00			

Table 5 – Characteristics of radial modified wave functions $\tilde{R}_{2l}^{mod}(r)$

J^π, $\tilde{R}_{2l}^{mod}(r)$	r_m, fm	$C_{2\ell}$	N	P_{out}, %
$1/2^+$, $\tilde{R}_{2s}^{mod}(r)$	6,669	0,278476	0,940277	24,9
	8,604	0,181369	0,967572	20,1
$5/2^+$, $\tilde{R}_{2d}^{mod}(r)$	4,946	3,759468	0,979647	15,7
	11,393	0,584071	0,958564	10,5
$3/2^+$, $\tilde{R}_{2d}^{mod}(r)$	7,218	0,584214	0,986567	10,8

Table 5 is a short summary on the general characteristics of the obtained modified radial functions $\tilde{R}_{2l}^{mod}(r)$. Let us pay attention to the probability of the localization of the valence neutron out of the mean square area of the core ^{12}C given as $P_{out}(\%)$. Comparison of these values make it possible to conclude that $1/2^+$ state is the halo one, but states $5/2^+$ and $3/2^+$ are likely belong to the skin structure states.

Modified functions in impulse representation

Due to the Heisenberg uncertainty relation "coordinate-momentum" all modifications of the wave functions at large distances must, first of all reflected in the momentum distributions for small values q.

The corresponding analytical expressions for the oscillator and modified functions obtained on the base of (13) in impulse representation for the case $J^\pi = 1/2^+$ are:

$$R_{2s}(q) = r_0^{3/2}\frac{\sqrt{6}}{\pi^{1/4}}\cdot\left(1-\frac{2q^2r_0^2}{3}\right)e^{-\frac{q^2r_0^2}{2}} \qquad (15)$$

$$R_{2s}^{\mathrm{mod}}(q) = \frac{\sqrt{\pi}}{4}\sum_{i=1}^{15}B_i\cdot\frac{1}{\beta_i^{3/2}}e^{-\frac{q^2}{4\beta_i}}. \qquad (16)$$

For excited states $5/2^+$ and $3/2^+$ the analogue expressions for the oscillator and modified functions on the base of (14) have been obtained

$$R_{2d}(q) = r_0^{3/2}\frac{4}{\pi^{1/4}\sqrt{15}}\cdot q^2r_0^2e^{-\frac{q^2r_0^2}{2}} \qquad (17)$$

$$R_{2d}^{\mathrm{mod}}(q) = \frac{\sqrt{\pi}}{16}\sum_{i=1}^{15}D_i\cdot\frac{q^2}{\gamma_i^{7/2}}e^{-\frac{q^2}{4\gamma_i}}. \qquad (18)$$

It is natural to discuss the probability density constructed as squared functions (15)-(18) $\rho_{2l}(q) = \left|R_{2l}(q)\right|^2$. The results of calculations are given in Figures 1 – 3.

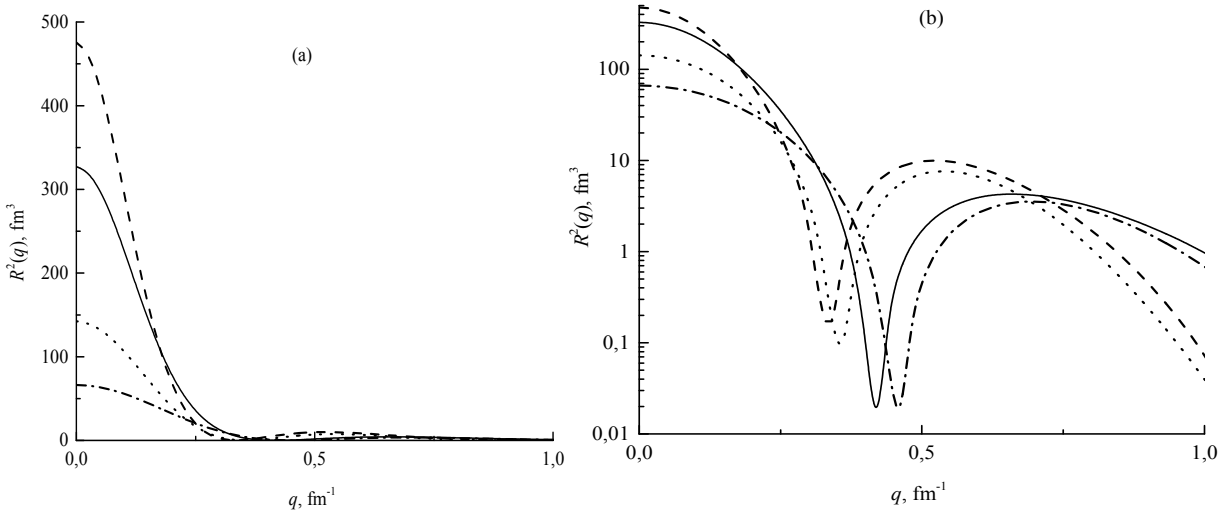

Figure 1 – Impulse distributions for excited $1/2^+$ state of ^{13}C: (a) – linear scale; (b) – logarithmic scale. Set №2: $\rho_{2s}^{\text{mod}}(q)$ – solid line, $\rho_{2s}(q)$ – dash-dot; set №1: $\rho_{2s}^{\text{mod}}(q)$ – long dash, $\rho_{2s}(q)$ – dots

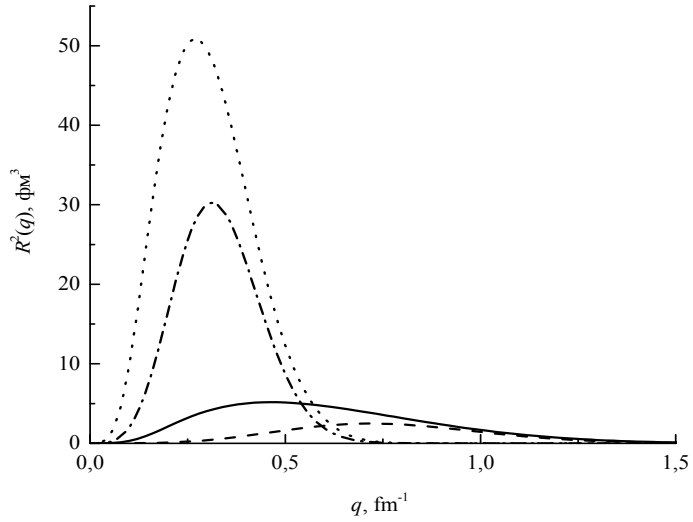

Figure 2 – Impulse distributions for excited $5/2^+$ state of ^{13}C. Set №2: $\rho_{2d}^{\text{mod}}(q)$ – solid line, $\rho_{2d}(q)$ – dash; set №1: $\rho_{2d}(q)$ – dash-dot, $\rho^{\text{mod}}(q)$ – dots

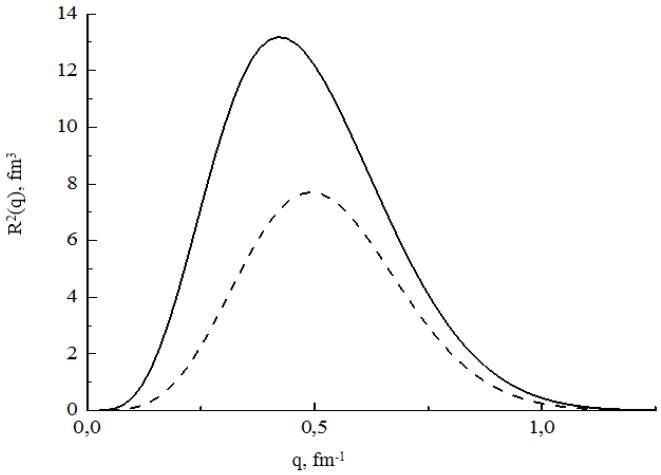

Figure 3 – Impulse distributions for excited $3/2^+$ state of ^{13}C. $\rho_{2d}^{mod}(q)$ – solid line, $\rho_{2d}(q)$ – dash

As can be clearly seen from Figure 1, in fact, in the region of small momentum transfers $q \to 0$ momentum distributions obtained for all functions differ drastically. Thus, our assumption is that this characteristic is sensitive to the modifications of the asymptotic behavior is fully confirmed.

Figures 2 and 3 correspond the nodeless functions. They are exactly equal to zero at $q = 0$. Such momentum distributions are compared by a well-known characteristic of the width at half-of – height maximum Γ. It is for the Γ values can be seen how wide or narrow impulse distributions, and, consequently, to draw conclusions about the asymptotic behavior of the length of the asymptotic in the coordinate representation.

Conclusion

Sufficiently general method of the modification of radial functions for the improving of the asymptotic behavior is presented. The coming ambiguities appearing while defining the oscillator parameters have been examined. The modified functions are presented as convenient expansion by Gaussian basis. The different versions of the modifications ***№1*** and ***2***, as well as purely oscillator functions significantly distanced themselves in the momentum representation. To address the issue of choice of reliable functions it is necessary in the future to compare the obtained results with the available experimental data on elastic and inelastic form factors.

References

1 I. Tanihata, S. Terashima, R. Kanungo. Observation of large enhancements of charge exchange cross section with neutron-rich carbon isotopes // Phys. Rev. – 2016. – Vol. 4 – P. 1-11.

2 P.G. Hansen. Nuclear halos // Rev. Nucl. Part. Sci. – 1995 – Vol. 45. – P. 591-634.

3 I. Tanihataa, H. Savajols, R. Kanungod. Recent experimental progress in nuclear halo structure studies // Prog. Part. Nucl. Phys. – 2013. – Vol. 68. – P. 215-313

4 W. Horiuchi, Y. Suzuki, B. Abu-Ibrahim. Systematic analysis of reaction cross section of carbon isotopes // Phys. Rev. – 2007 – Vol. C75 – P. 044607 – 1-14.

5 A.R. Samana, T. Tarutina, M.S. Hussein. Pairing correlations in odd-mass carbon isotopes and effect of Pauli principle in particle-core coupling in ^{13}C and ^{11}Be // Nuclear Physics – 2007 – Vol. A791. – P. 36-56.

6 T. L. Belyaeva, R. Perez-Torres, A. S. Demyanova et al. Neutron asymptotic normalization coefficients and halo radii of the first excited states of ^{13}C and ^{11}Be // Phys. Rev. – 2014. – Vol. 90 – P. 1-2.

7 Lin Cheng-Jian et al. Extraction of the rms radius of ^{13}C from asymptotic normalization coefficients // Chinese Phys. Lett. – 2001. – Vol. 18. – P. 1446-1448.

8 W. Nortershauser, D. Tiedemann, M. Zakov et al. Nuclear Charge Radii of $^{7,9,10}Be$ and the one-neutron halo nucleus ^{11}Be // Phys. Rev. Lett. – 2009. – Vol. 102. – P. 062503.

9 S.B. Dubovichenko. Thermonuclear Processes of the Universe. // First English edition. NOVA Sci. Publ. New York. – 2012. – P.194.

10 F. Cartoiu, L. Trache, C.A. Gagliardi et al. Radii of halo states in light nuclei deduced from ANC // Romanian Reports in Physics. – 2007. – Vol. 59. No. 2. – P. 357–375.

11 N. K. Timofeyuk, P. Descouvemont. Relation between widths of proton resonances and neutron asymptotic normalization coefficients in mirror states of light nuclei in a microscopic cluster model. // Phys. Rev. Lett. – 2013. – Vol. 91. – P. 2325019.

12 M. Abramowitz, I.A. Stegun. Handbook of Mathematical Functions. Washington: Nat. Bur. Stand. – 1964. – P. 104

UDC 536.46.:532.517.4

Simulation of the aerodynamics and combustion of a turbulent pulverized-coal flame

Pilipenko N.V.

Faculty of Physics and Engineering, St. Petersburg National Research University of Information Technologies, Mechanics, and Optics (ITMO), Lomonosova 9, 191002 St. Petersburg, Russia
e-mail: pilipenko38@mail.ru

Using the three-dimensional modeling method, numerical experiments on flame combustion of pulverized-coal fuel have been performed. The results of a three-dimensional numerical simulation of flow aerodynamics, temperature and carbon oxides are presented. Studies have been carried out for a pulverized-angle flame of various dispersity.In the study of a wide range of modern problems of science and technology, numerical simulation of heat and mass transfer process is particularly important and has enormous practical application. Interaction of reacting flows is described by a complex system of nonlinear partial differential equations. Indispensable effective method of theoretical study of such flows is a numerical simulation.

Key words: simulation, coal combustion, aerodynamics, monodisperse flame, polydisperse flame, concentration fields.
PACS number(s): 47.27, 47.70.Pq

Introduction

Numerical modeling is sufficiently accurate and inexpensive way to analyze complex processes that occur during combustion of the fuel in the combustion chambers of real power plants, and it allows to simultaneously consider the complex of processes that are almost impossible to do, conducting in situ experiments. Only the numerical modeling and carrying out computational experiments optimally solve scientific and project engineering tasks in this area (improvement, design of new boilers; burners upgrade; development of multistage fuel combustion systems, optimization of combustion processes and other) [1,2].

At the present stage of development of the energy industry, immediate consideration and resolution of environmental issues are required. Due to the fact, that for most countries the main sources of pollutant emissions into the atmosphere are companies operating in the burning of low-quality raw materials as well as with poorly equipped with flue gas cleaning systems, the problem of pollution of the Earth's atmosphere is an urgent. Environmentally hazardous emissions, which are products of coal combustion [3-5] reactions cause enormous damage to the earth's ecosystem. It is therefore necessary to carry out a detailed study of physical and chemical processes that occur during combustion of energy fuels and to solve the problem of environmentally "pure" making use of coal [6, 7].

Methodology of investigation

For carrying out computational experiment the combustion chamber of the real power boiler BKZ-160 Almaty TPP-3 (Kazakhstan) was selected. The boiler BKZ-160 of drum-type furnace with dry slag removal has a calculated steam generating capacity 160 t/h at a pressure of 9.8 MPa and a temperature of the superheated steam 540 ^{0}C. The boiler has a U-shaped profile with a rectangular prism furnace. Combustion chamber volume is 790 m3. On the sides of the combustion chamber located four blocks direct flow slot burners (two burners in the block) which directed at a tangent to the circle with a diameter of one meter. Each burner has a fuel mixture channel and two secondary air channel, they are located from above and from below the channel of air-fuel mixture, and divided lined piers. The top and bottom burners are also divided by a pier. In the center of burners is located oil-fired nozzle for lighting and lighting of the flame. The performance of each of the eight coal-fired burner fuels is 4 t/h.

Computational experiments on research heat and mass transfer processes have been carried out by the starting FLOREAN [8] software package, the geometry of the combustion chamber was created by

a computer program «PREPROZ» (Figure 1b). The software package FLOREAN was created to solve problems in the field of burning solid fuel and was repeatedly tested in many modern studies [1-12]. During the numerical simulation of heat and mass transfer process, the control volume method has been applied. Combustion chamber of a power boiler BKZ-160 has been divided into control volumes; it is possible to obtain 217536 computational areas.

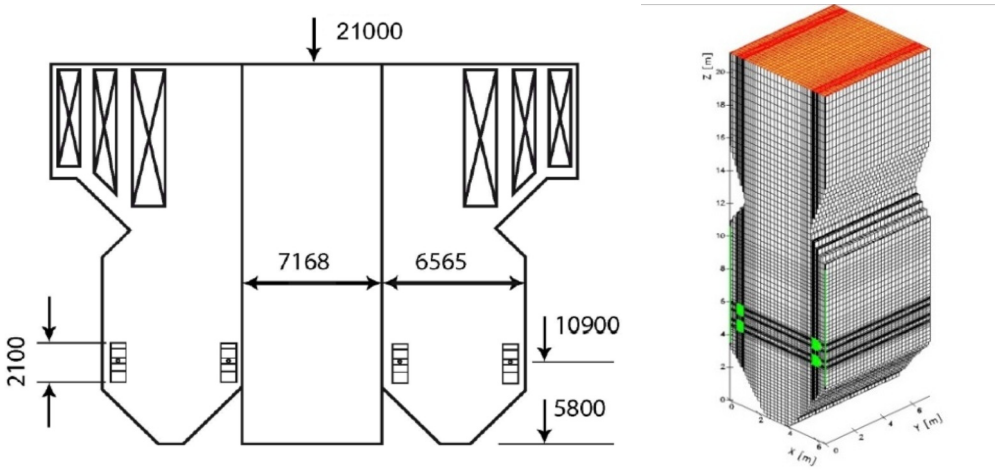

Figure 1 – a) Scheme of the furnace, b) General view of the camera, broken down into control volumes

Numerical simulation was carried out on the basis of solutions of the Navier-Stokes equations, equations of heat diffusion and diffusion of components of the reacting mixture and the reaction products based on thermal radiation and multiphase media, equations of state, and chemical kinetics equations defining the intensity of nonlinear energy and matter [8, 13-15].

For a qualitative description of combustion processes in a real three-dimensional physical and chemical system (combustion chamber of Thermal power plant) in the present work a numerical calculation of a turbulent pulverized coal flame was carried out taking into account the dispersion of coal. The percentage distribution of carbon particles in size: d_p=10 mkm – 10%; d_p=30 mkm – 20%; d_p=60 mkm – 40%; d_p=100 mkm – 20%; d_p=120 mkm – 10% corresponds to a polydisperse flame, d_p=60 mkm – 100% – is the averaged diameter, which corresponds to a monodisperse flame. Numerical calculation in the work was carried out for the two cases listed above.

Results of numerical simulation

Let us consider the profiles of aerodynamics combustion of a turbulent pulverized flame in different sections along the length of the flame. Figure 2 shows the distribution of the full-velocity vector in the longitudinal section of the furnace during combustion of a monodisperse and polydisperse flames. Obtained velocity fields allow us to visually analyze the aerodynamics of reacting flows in the combustion chamber. The fields of the full-velocity vector show the value of the flow velocity of the medium and its direction at each point.

In the Figure 2 the area of fuel and oxidizer is clearly visible: counter dust and gas streams from opposing tangential burners create a vortex in the central part on the location of burners and level of active burning zone. Clearly visible is the recirculation zone with reverse gas currents [15]. Part of the flow is directed down to the funnel, forming two symmetrical vortex in the area below the burner arrangement, it is typical both for burning of a monodisperse flame and for burning of a polydisperse flame. However, in a longitudinal section of the combustion chamber symmetry is broken relative to the vertical axis of the chamber when burning polydisperse flame (Figure 2b). It means that burning of dust and gas streams with different particle sizes affects to the character of the flow stream.

In cross-section chamber at a level between the lower and upper tiers of burners there is a clear picture of the current (Figure 3). The pulverized coal streams flowing into the chamber deviate from the direction of the burner axes (located tangentially) towards the adjacent walls, with which they make up a smaller angle. Fusing into the total flow, the jets create a volumetric vortex with a vertical axis of rotation, which, as it rises, untwists and then moves along the axis, as can be seen clearly in Figure 2.

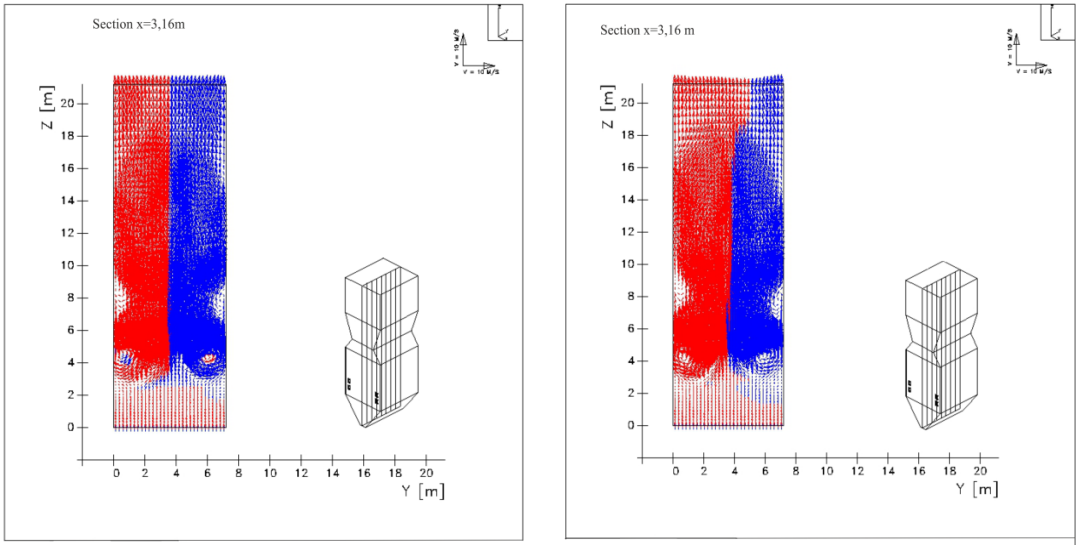

a) b)

Figure 2 – Field of a vector of full velocity in the longitudinal section of the combustion chamber (x = 3.16 m) for a) monodisperse flame; b) polydisperse flame

\

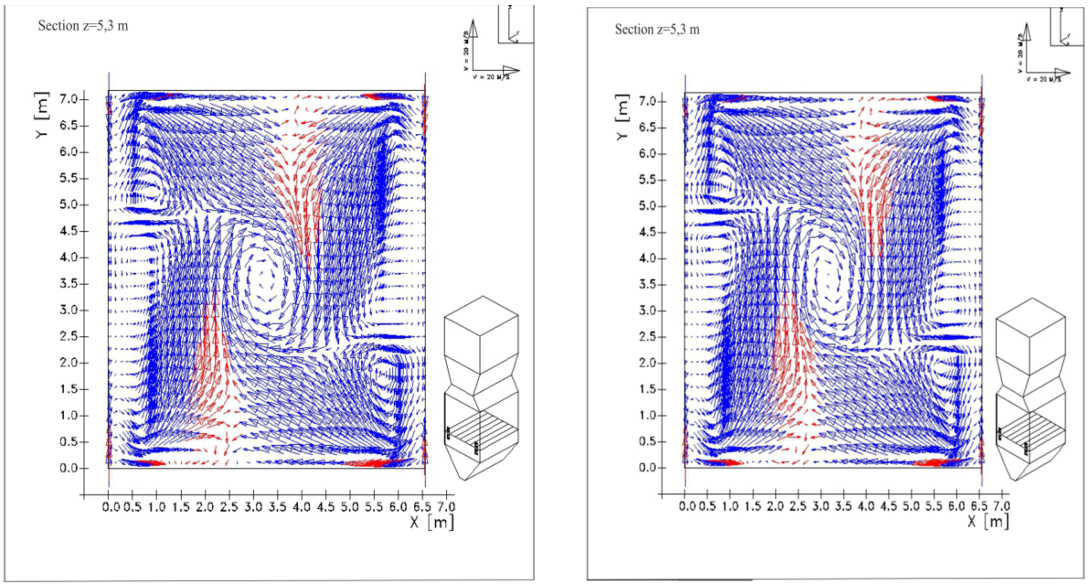

a) b)

Figure 3 – Field of a vector of full velocity in the cross-section of the combustion chamber (z = 5.3m) for a) monodisperse flame; b) polydisperse flame

The central vortical motion of the pulverized coal stream leads to uniform heating of the combustion chamber walls, to a decrease in the slagging of the heat shields and heat losses, which prolongs the life of individual elements of the boiler plant, and also increases the heat removal surface, which speaks of the advantages of the furnaces with the tangential arrangement of the burners. The aerodynamics of flow in the combustion of monodispersed and polydispersed flames has some differences; however, if it is necessary to make quick estimates, in numerical simulation of the aerodynamic characteristics of the coal combustion process, one can use the model of burning a particle of averaged size, which in turn reduces the expenditure of computer time [1, 16-21].

Being the UNFCCC framework (the United Nations Framework Convention on Climate Change) since 1995 and the Kyoto Protocol since 2009, Kazakhstan has a principled position and pursues a consistent policy in the field of preventing global climate change, in the field of reducing the carbon intensity of the economy and in the field increasing energy efficiency, creating conditions for the transition to technologies for environmentally "pure" burning of energy fuel [22]. In this connection, the study of the concentration characteristics of greenhouse gases is an urgent task. Figures 4, 5, 7 show a comparative analysis of carbon oxide concentration distributions for the case of a polydisperse and monodisperse flare.

Analyzing the Figure 4 it can be argued, the nature and pattern of carbon monoxide CO and carbon dioxide CO_2 are different from each other. Concentration of carbon oxide reaches area of the maximum values in a zone of active burning, unlike carbon dioxide which concentration increases as it moves out of the combustion chamber.

Concentrations of poly- and monodisperse flames in the field of an arrangement of burners do not differ. The average value of the concentration of carbon monoxide for polydisperse flame in the first tier of burners (z= 4,81m) is $0{,}184 \cdot 10^{-2}$ kg/kg, for monodisperse is $0{,}185 \cdot 10^{-2}$ kg/kg, in the second tier (z = 5,79m) is $0{,}279 \cdot 10^{-2}$ kg/kg both for poly- and for monodisperse flames (Figure 4a). In the area of active burning the concentration of carbon monoxide CO reaches the maximum value, chemical processes of formation of carbon monoxide CO fade to output from the combustion chamber, for polydisperse flame at the exit of the combustion chamber the mean value is 1,35·10- 4 kg/kg, for monodisperse is 0,61 10- 4 kg/kg (Figure 4a).

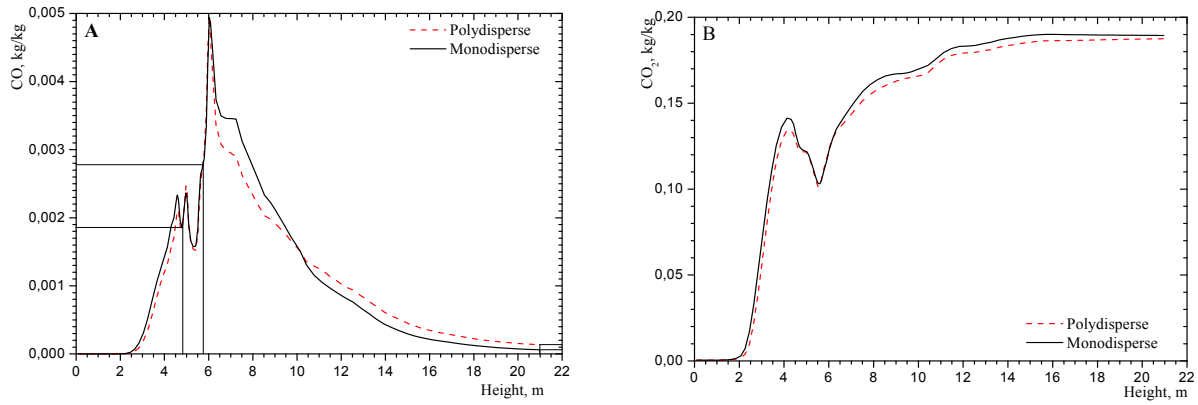

Figure 4– Comparison of the average values of concentration CO (A) и CO_2 (B) for poly- and monodisperse flame on height of the combustion chamber

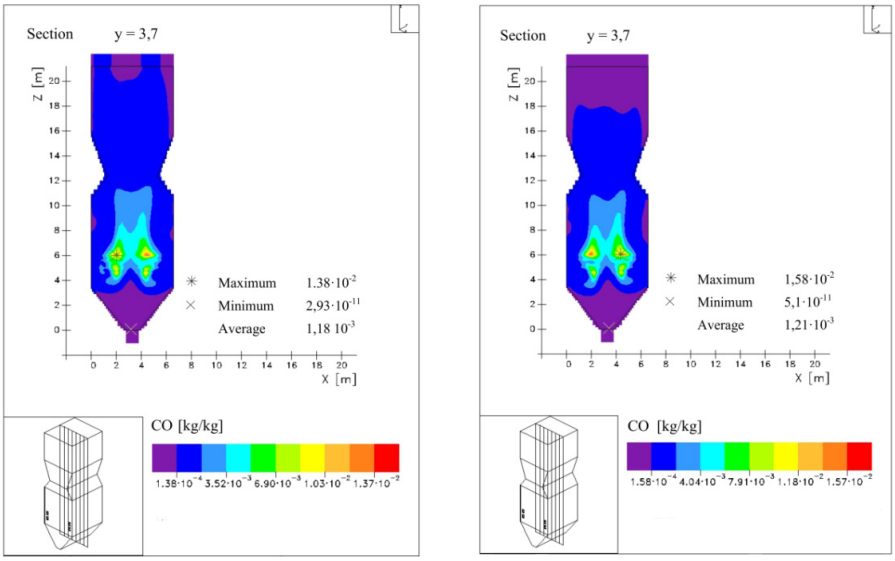

a) b)

Figure 5 – Distribution of the carbon oxide concentrati on in the longitudinal section of the furnace combustion chamber (y = 3.7m) for a) monodisperse flame; b) polydisperse flame

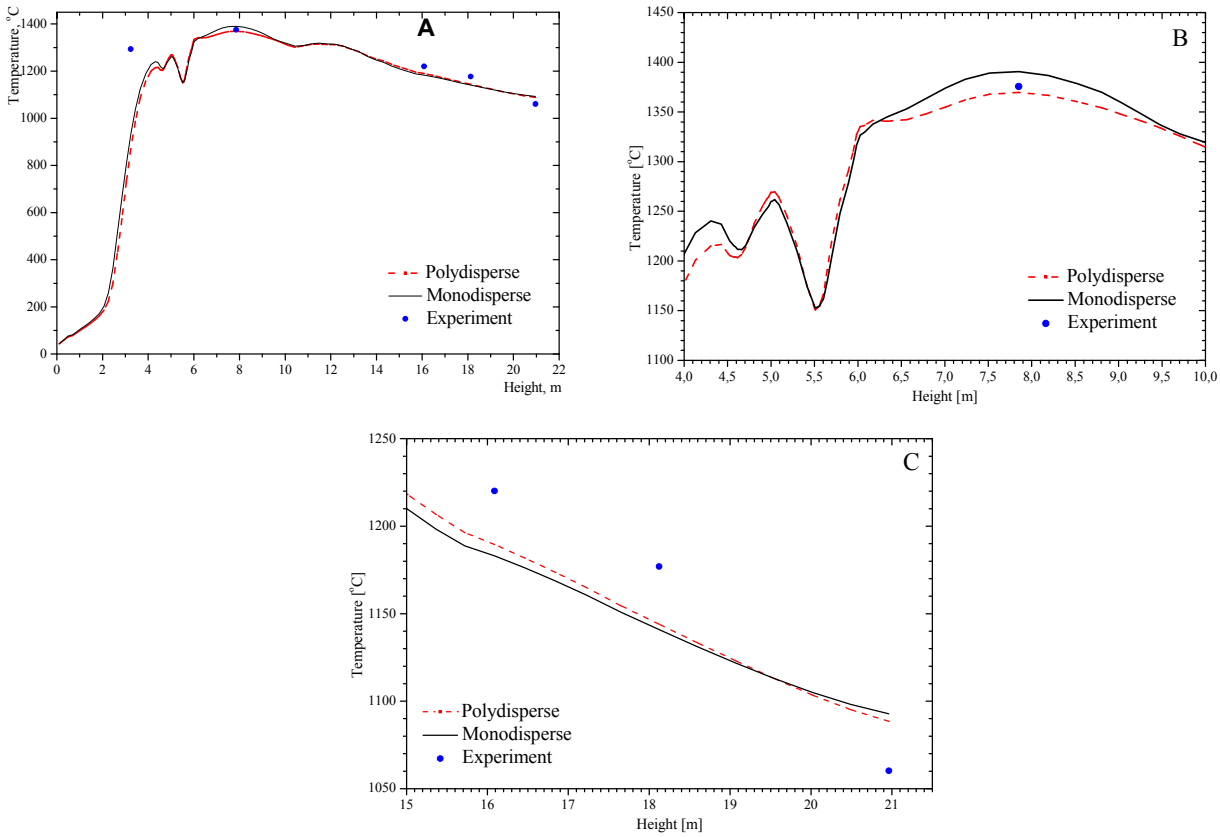

Figure 6 – Comparison of average temperature values for poly- and monodisperse flames and a comparison with the field experiment [23]: A) on height of the combustion chamber B) zone of active burning C) at the outlet of the combustion chamber

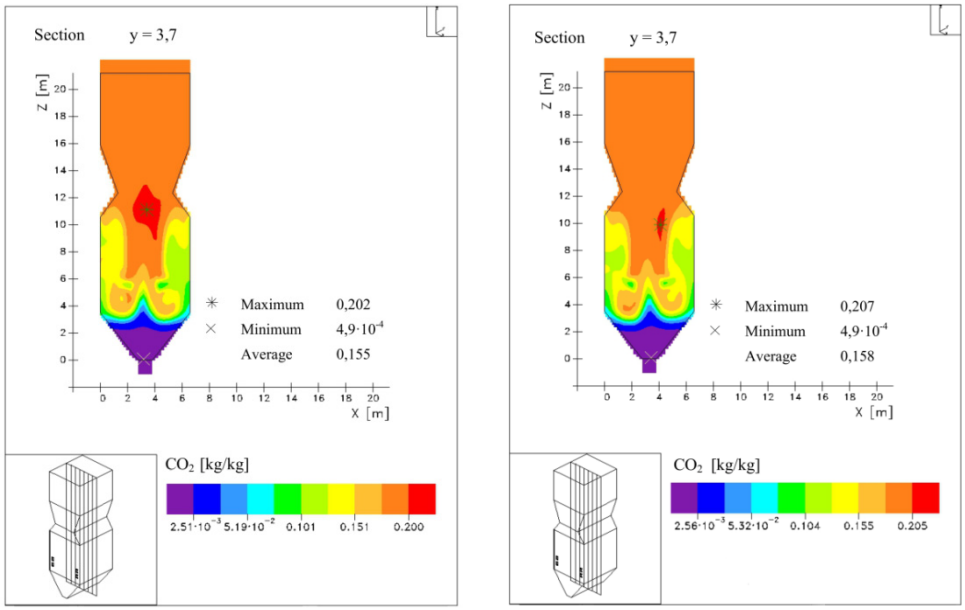

a) b)

Figure 7 – Distribution of carbon dioxide concentration in a longitudinal section of the combustion chamber of the combustion (y = 3.7m) for a) monodisperse flame; b) polydisperse flame

Analyzing the distribution of CO concentration in the longitudinal sections of the combustion chamber (Figure 5), it can be said that in the active combustion zone, there is a clear difference in the formation of CO for a mono- and polydisperse flames, which indicates that the particle size has a significant effect on the formation of reaction products. The maximum values of carbon monoxide CO are explained by the intensive physico-chemical interaction between the fuel carbon and air oxygen, and with increased temperatures in this region (Figure 6).

Figure 6 shows the experimental points obtained directly from measurements at the termal power plant [23]. It is confirmed that the numerical simulation results are in good agreement with the results of a natural experiment. It is leading to the conclusion of the applicability of the proposed physical-mathematical model of combustion processes, used in the present work. It should also be noted that the experimental data obtained directly from TPP-3 lie closer to the temperature curve of the polydisperse flame, from which it can be argued that the polydisperse flame model is more sensitive and reflects a more real process of burning pulverized coal at Almaty TPP-3.

Analyzing Figures 4b, and 7 it can be said that as flow moves out of the combustion chamber CO_2 is restored from CO, this regularity is fair both for monodisperse, and for polydisperse flames. It is possible to determine value of concentration in any point of furnace by a color scale of the received figures which is not always possible to obtain during the field experiments on the thermal power plant. So the average values of carbon dioxide CO_2 in the longitudinal section of the combustion chamber (y = 3,7m) for polydisperse flame is 0.155 kg/kg, for monodisperse flame is 0.158 kg/kg (Figure 7). At the exit of the combustion chamber average concentration of carbon dioxide for polydisperse flame is 0.1876 kg/kg, for monodisperse flame is 0.1895 kg/kg.

Conclusion

In the present work, the calculation of aerodynamics, thermal and concentration characteristics of the combustion of mono- and polydisperse flames is performed; the results of the study can formulate the following conclusions:

1. A detailed picture of the structure of the flame is obtained, which includes a developed recirculation zone with return currents of the combustion products;

2. It is noted that the character of formation of the concentration fields CO and CO_2 is different. The maximum concentration of carbon monoxide reaches in the zone of active combustion, and the

formation of carbon dioxide CO_2 increases as it moves towards the outlet from the furnace;

3. The results of computer simulation of temperature T, were compared with the results of field experiments, the analysis of which confirms the correctness of the chosen model of numerical experiment.

In conclusion, we note that the nature of combustion of mono- and polydisperse dust has differences, i.e. The influence of fineness of grinding has a significant influence on the processes of heat and mass transfer in the combustion chamber of CHPP boilers. The combustion model of polydisperse dust more accurately reflects the actual combustion process, which confirms the comparison with the full-scale experiment. However, the application of this model requires large computer, time resources.The results obtained in this study will give recommendations for optimizing the burning process of pulverized coal in order to reduce pollutant emissions and creations of power stations on 'pure' and an effective utilization of coal.

References

1. A. Bekmukhamet, S. A. Bolegenova, M. T. Beketayeva et al. Numerical modeling of turbulence characteristics of burning process of the solid fuel in BKZ-420-140-7c combustion chamber// International Journal of Mechanics. – 2014. – Vol. 8. – P. 112-122.

2. A. Askarova, V. Maximov, A. Ergalieva et al. 3-D modeling of heat and mass transfer during combustion of solid fuel in Bkz-420-140-7C combustion chamber of Kazakhstan // Journal of Applied Fluid Mechanics. – 2016. – Vol. 9. – P.699-709.

3. N. V. Pilipenko, I. A. Sivakov. A method of determining nonstationary heat flux and heat conduction using parametric identification// Measurement Techniques – 2011. – Vol.54. – P. 318-323.

4. N. V. Pilipenko. The systematic errors in determining the nonstationary heat-exchange conditions with parametric identification// Measurement Techniques – 2007. – Vol.50. – P. 880-887.

5. A. S. Askarova, A. Bekmuhamet, V. Yu. Maximov et al. Mathematical simulation of pulverized coal in combustion chamber // Procedia Engineering. – 2012. – Vol.42. – P.1259-1265.

6. S. A. Bolegenova, V. Yu. Maximov, Z. Kh. Gabitova et al. Computational method for investigation of solid fuel combustion in combustion chambers of a heat power plant // High Temperature. – 2015. – Vol. 53. – P. 792-798.

7. M. Beketayeva, Sh. Ospanova, Z. K. Gabitova. Investigation of turbulence characteristics of burning process of the solid fuel in BKZ 420 combustion chamber // WSEAS Transactions on Heat and Mass Transfer. – 2014. – Vol.9. – P. 39-50.

8. H. Müller. Numerische Berechnung dreidimensionaler turbulenter Strömungen in Dampferzeugern mit Wärmeübergang und chemischen Reaktionen am Beispiel des SNCR–Verfahrens und der Kohleverbrennung: Fortschritt–Berichte VDI–Verlag . – 1992. – Vol. 6. – P. 158.

9. S. Bolegenova, S. Bolegenova, A. Bekmukhamet et al. Numerical experimenting of combustion in the real boiler of CHP// International Journal of Mechanics. – 2013. – Vol. 7. – P. 343-352.

10. A. Askarova, M. Beketeyeva, P. Safarik et al. Numerical modeling of pulverized coal combustion at thermal power plant boilers// Journal of Thermal Science. – 2015. – Vol. 24. – P. 275-282.

11. Ye. I. Lavrichsheva, R. Leithner, H. Müller, A. Magda et al. Combustion of low-rank coals in furnaces of Kazakhstan coal-firing power plants // VDI Berichte. – 2007. – Vol. 1988 – P. 497-502.

12. Yu. E. Karpenko, V. E. Messerle, A. B. Ustimenko. et al. Mathematical modelling of the processes of solid fuel ignition and combustion at combustors of the power boilers // 7th International Fall Seminar on Propellants. Explosives and Pyrotechnics . Xian. – 2007. – Vol. 7. – P. 672-683.

13. R. Leithner. Numerical Simulation. Computational Fluid Dynamics CFD: Course of Lecture. Braunschweig. – 2006. – P. 52.

14. S. Vockrodt, R Leithner, A. Schiller et al. Firing technique measures for increased efficiency and minimization of toxic emissions in Kasakh coal firing // VDI . 19th German Conference on Flames. Germany. VDI Gesellschaft Energietechnik. Verein Deutsch Ingenieure. Combustion and Incineration. VDI Berichte. – 1999. – Vol. 1492. – P.93-97.

15. A. S. Askarova, S.A. Bolegenova, V.Y. Maximov et al. Numerical research of aerodynamic characteristics of combustion chamber BKZ-75 mining thermal power station // Procedia Engineering. – 2012. – Vol.42. – P. 1250-12-59.

16. M. A. Buchmann, A. Askarova. Structure of the flame of fluidized-bed burners and combustion processes of high-ash coal // Gesellschaft Energietechnik. Combustion and Incineration - Eighteenth Dutch-German Conference on Flames. VDI Berichte. – 1997. – Vol.1313. – P. 241-244.

17. E. I. Karpenko, V. E. Messerle, A. B. Ustimenko. Plasma enhancement of combustion of solid fuel // Journal of High Energy Chemistry. – 2006. – Vol. 40. – P.111-118.

18. V. E. Messerle, A. B. Ustimenko, V. Yu. Maksimov et al. Numerical simulation of the coal combustion processinitiated by a plasma source // Thermophysics and Aeromechanics. – 2014. – Vol. 21. – P. 747-754.

19. A. S. Askarova, V. E. Messerle, A. B. Ustimenko et al. Numerical simulation of pulverized coal combustion in a power boiler furnace //High Temperature. – 2015. – Vol. 53. – P. 445-452.

20. M. Gorokhovski, A. Chtab-Desportes, I. Voloshina, A. Askarova. Stochastic simulation of the spray formation assisted by a high pressure // AIP Conference Proceedings. Xian. – 2010. – Vol. 1207. – P. 66-73.

21. E. I. Heierle, S. A. Bolegenova, V. Ju. Maximov, S. A. Bolegenova, R. Manatbayev, M. T. Beketaeva, A. B. Ergalieva. CFD study of harmful substances production in coal-fired power plant of Kazakhstan // Bulgarian Chemical Communications. – 2016. – Special Issue E. – P. 260-265.

22. N. V. Pilipenko, D. A. Gladskikh. Determination of the Heat Losses of Buildings and Structures by Solving Inverse Heat Conduction Problems // Measurement Techniques. – 2014. – Vol.57. – P. 181-186.

23. B. K. Alijarov, M. B. Alijarova. Combustion of Kazakh Coals in Thermal Power Stations and Large-Power Boiler Houses. Almaty. – 2011. – P. 306. (in Russian).

UDC 538.97; 539.216.2; 539.23, 620.91:662.97

Investigation of SiC and C nanostructures synthesized by the method of chemical vapor deposition on Ni films

[1,2]Kenzhegulov A.K., [1]Mansurov B.Z., [1,2*]Medyanova B.S., [1,2]Partizan G., [1,2]Suyundykova G.S., [1,2]Zhumadilov B.E., [3]Koztayeva U.P., [4]Xin Jiang

[1]*Center for Innovative Technologies of the Institute of Combustion Problems, 050050, Polezhaeva str., 20, Almaty, Kazakhstan*
[2]*Al-Farabi Kazakh National University, Faculty of Physics and Technology, 050040, al-Farabi ave., 71, Almaty, Kazakhstan*
[3]*Institute of Nuclear Physics, 050032, Ibragimova str., 1, Almaty, Kazakhstan*
[4]*Institute of Materials Engineering, University of Siegen, Paul-Bonatz-Straße 9-11, 57076, Siegen, Germany*
[*]*e-mail: bota2192@mail.ru*

The paper presents the results of experiments on synthesis of SiC and C nanostructures by the method of microwave plasma assisted chemical vapor deposition on Ni films. The plates of polished single-crystal and porous silicon were used, on the surface of which a thin layer of Ni was deposited.
The dependence of the structure and morphology of the samples on the plasma power is studied. Scanning electron microscopy has shown that the formed nanostructures have a diameter of 100-170 nm and a rough surface. Analysis of the results showed that, the growth of nanostructures on the surface of porous silicon is more massive in contrast to polished Si.
The structure of the obtained samples and its dependence on the plasma power were studied by Raman scattering. The results of studies showed the presence of silicon carbide nanostructures with 3C-SiC polytype structure. Also, the main carbon peaks in the range of ~1300 and ~1500 cm^{-1}, which correspond to carbon nanostructures were found on both types of substrates.

Key words: silicon carbide and carbon nanostructures, chemical vapor deposition, microwave plasma, porous silicon.
PACS: 68.60.−p, 88.85.M

Introduction

Nanostructuring of silicon carbide (SiC) allows changing many of its physical properties, for example, mechanical elasticity in comparison with bulk material [1]. Other interesting properties of SiC nanostructures (NS) include the presence of field emission, the threshold and properties of which are comparable to that demonstrated by carbon nanotubes [2]. These and many other properties make silicon carbide NS extremely attractive for research.

Filamentous SiC crystals, like carbon nanotubes, have a high ratio of length to diameter (100-200 and more), the diameter of crystalline SiC fibers can vary considerably from 40 to 200-500 nm [3]. The filamentary form provides improved mechanical properties of whiskers [4]. In addition to the traditional use as components of ceramics and structural materials, SiC whiskers are of interest for the development of new components of high-temperature electronic devices. Advantages of using SiC in this area are associated with its high thermal and corrosion resistance, combined with the large value of the forbidden zone (2.4-3.3 eV, depending on the polytype of silicon carbide) [5].

The paper presents the results of experiments on synthesis of SiC and C nanostructures by the method of microwave plasma assisted chemical vapor deposition on Ni films. As a result of studies, the dependence of the plasma power and type of substrate on the structure and morphology of the obtained samples was studied.

Experimental

Preparation of substrates

Single-crystal silicon wafers (analogue of SHB-20 brand, manufactured by Siegert Wafer GmbH, Germany) with dimensions of 1×1 cm with orientation [100] and [111] were used as substrates and basis for nickel films.

In order to activate the surface during synthesis, substrates of porous silicon (PS) were prepared at The Educational Laboratory of Semiconductor Instrumentation of Faculty of Physics and Technology of KazNU (Almaty, Kazakhstan). The crystalline silicon was pretreated in acetone and

placed in a solution of H_2SO_4:H_2O_2 for 5 minutes, followed by washing in deionized water. The plates were then immersed in HF:H_2O etch for 1 minute, after which they were thoroughly washed. The PS was formed by electrochemical anodizing in a modified solution of composition HF (45%):ethoxyethanol:water in the ratio 1:2:1. The current density and anodization time were, respectively, 15 mA and 10 minutes. After etching, PS samples were thoroughly washed in deionized water and dried in air with lighting using a red lamp for 5 minutes.

Figure 1 shows electron microscopic images of PS surface.

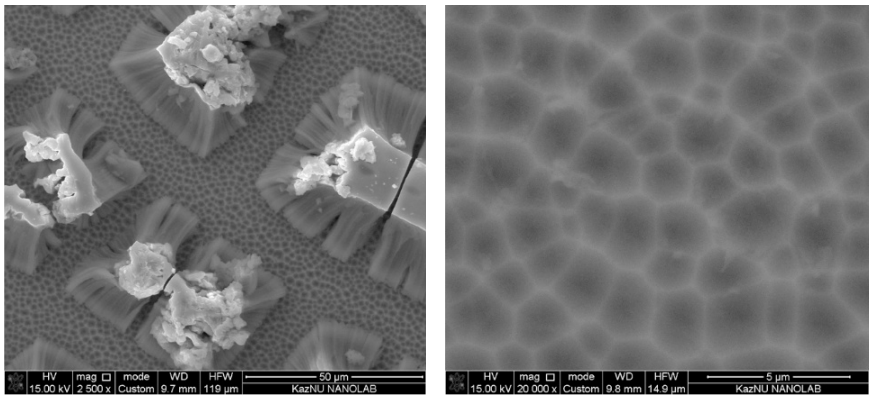

Figure 1 – Electron microscopic images of PS surface

Ni films were deposited by magnetron sputtering at a constant current in equipment VUP-5M for 5 minutes. Sputtering was carried out in a flow of working gas Ar at a pressure of 10^{-2} Torr. The Ar flow rate was 6 cm^3/min and was controlled by gas flow controller MCV-500SCCM. The experiments were carried out at a voltage on the target of 600 V and plasma current of 30 mA.

Synthesis of nanostructures

Synthesis of NS was carried out in the Department of Surface and Technology of New Materials of the Institute of Materials Engineering of the University of Siegen, Germany, on equipment of microwave plasma assisted chemical vapor deposition (MWCVD) of ASTEX system (frequency 2.45 GHz).

Prior to the experiments, substrates were purified with ethanol and then washed with distilled water, drying was carried out at room temperature. The plasma power varied from 1600 to 2200 W in 200 W steps. Depending on the power, the substrate temperature was varied from 600 to 900°C and measured with infrared pyrometer of Chino IR-AP M0011 model (Japan). The pressure in the chamber changed depending on the power to stabilize the plasma. Table 1 shows parameters of the experiments.

The experiments were carried out in atmosphere of a mixture of gases of trimethylsilane ($(CH_3)_4Si$) and hydrogen, the flow rate of which was 10 and 400 cm^3/min, respectively. The duration of all experiments is 120 minutes, the substrates are Ni on polished (Ni/Si) and porous (Ni /PsSi) Si of different orientations.

Table 1 – Parameters of the experiments

Substrate		Si orientation	Power plasma, W	Substrate temperature, °C	Pressure, Torr
Ni/Si	Polished	[100]	1600	600	40
			1800	700	47
			2000	800	50
			2200	900	57
	Porous	[111]	1600	600	40
			1800	700	47
			2000	800	50
			2200	900	57

Results and discussion

The obtained samples were studied by the methods of Raman scattering and scanning electron microscopy (SEM). Raman studies were carried out at the National Nanotechnology Laboratory of open type (Almaty, Kazakhstan) using spectrometer NT-MDT NTegra Spectra (laser wavelength λ = 473 nm). Analysis of samples by SEM was carried out at the Institute of Materials Science of the University of Siegen. To study the morphology and elemental analysis of samples, high-resolution scanning electron microscope of Gemini Ultra 55 model of Zeiss company with device for X-Ray spectral microanalysis from Thermo Scientific was used.

NS synthesized on substrates Ni/PSSi (100) and Ni/Si (100)

Figure 2 shows results of studies of samples synthesized at a substrate temperature of 600°C.

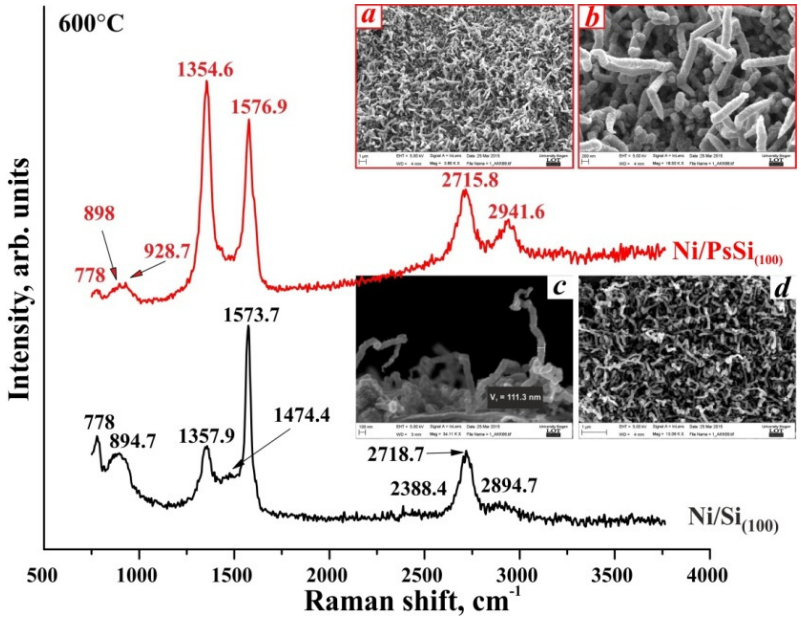

Figure 2 – Raman spectra and SEM images of samples synthesized at a substrate temperature of 600°C: *a, b* - Ni/PSSi$_{(100)}$; *c, d* - Ni/Si$_{(100)}$

Samples contain shifted silicon carbide peaks characteristic of 3C-SiC polytype structure, which are in the range of 778 and 898.1-928.7 cm^{-1}. Displacement can occur due to the presence of another crystalline structure, i.e. silicon carbide nanofibers [6]. The main carbon peaks are located in the region of 1354.6, 1576.9 cm^{-1} and 1348.1, 1573.7 cm^{-1}. The intensity of *D* peak and the presence of *D* + *G* peak in the region of 2941.6 cm^{-1} in the samples obtained on porous substrates indicate the defectiveness of the nanostructures. The samples are crystalline, indicating the presence of 2*D* peak at 2715.8 cm^{-1} and 2718.7 cm^{-1}.

The growth of NS both for polished and porous Si has a massive character over the entire surface of the substrate (2*a, d*). The formed NS have a diameter of 100-120 nm (2*c*). It is seen that the formed NS have a rough surface on SEM images (2*b, c*). Energy dispersive X-Ray spectra (Figure 3) indicate that the ratio of carbon and silicon concentrations in NS is on polished Si ~0.5 and on PS ~0.7.

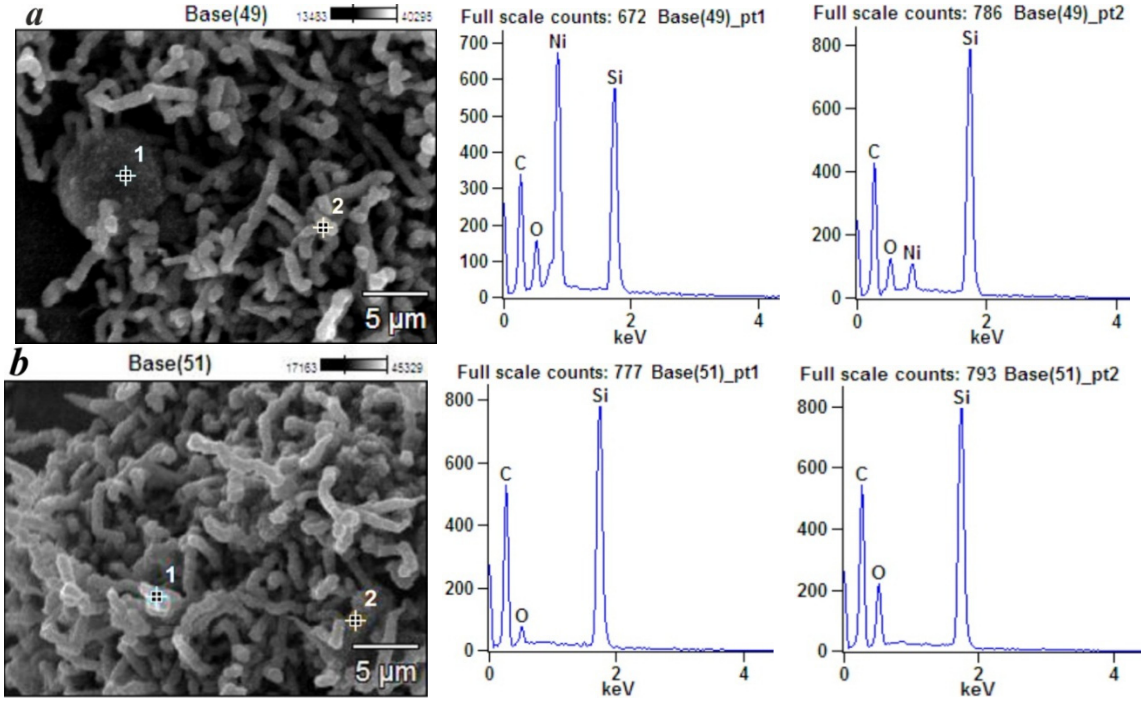

Figure 3 – Energy dispersive X-Ray spectra of samples synthesized at a substrate temperature of 600°C: *a* - Ni/Si$_{(100)}$; *b* - Ni/PSSi$_{(100)}$

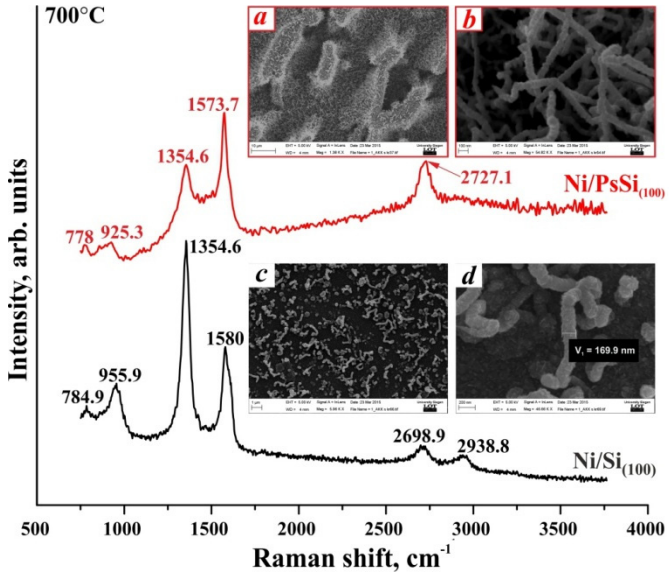

Figure 4 – Raman spectra and SEM images of samples synthesized at a substrate temperature of 700°C: *a, b* - Ni/PSSi$_{(100)}$; *c, d* - Ni/Si$_{(100)}$

Figure 4 shows Raman spectra and SEM images of samples obtained at a substrate temperature of 700°C.

In Figure 4, silicon carbide groups are also shifted to the low-frequency region of 771.2, 785 and 925.3, 955.9 cm^{-1}. The main carbon peaks are located within the limits of 1355-1358 and 1554.6-1580 cm^{-1}. Peaks of the second order in the region of 2699-2704.6 and 2960.9 cm^{-1}, which correspond to the groups 2*D* and *D* + *G*

are present in the high-frequency region of the spectrum. It can be assumed from intensity of *D* peak that nanostructures obtained on porous silicon substrate are less defective than nanostructures on polished substrates.

Figure 4 also shows SEM images of samples obtained at a substrate temperature of 700°C. As can be seen in Figure 4*d*, the synthesized NS have an average diameter of 100-170 nm. Figure 4b confirms that the growth of NS on PS surface is more massive than on polished Si. Energy dispersive X-Ray spectra (Figure 5) show that the ratio of carbon and silicon concentrations in NS is on polished Si ~ 0.5-0.7 and on PS ~ 0.3-0.5.

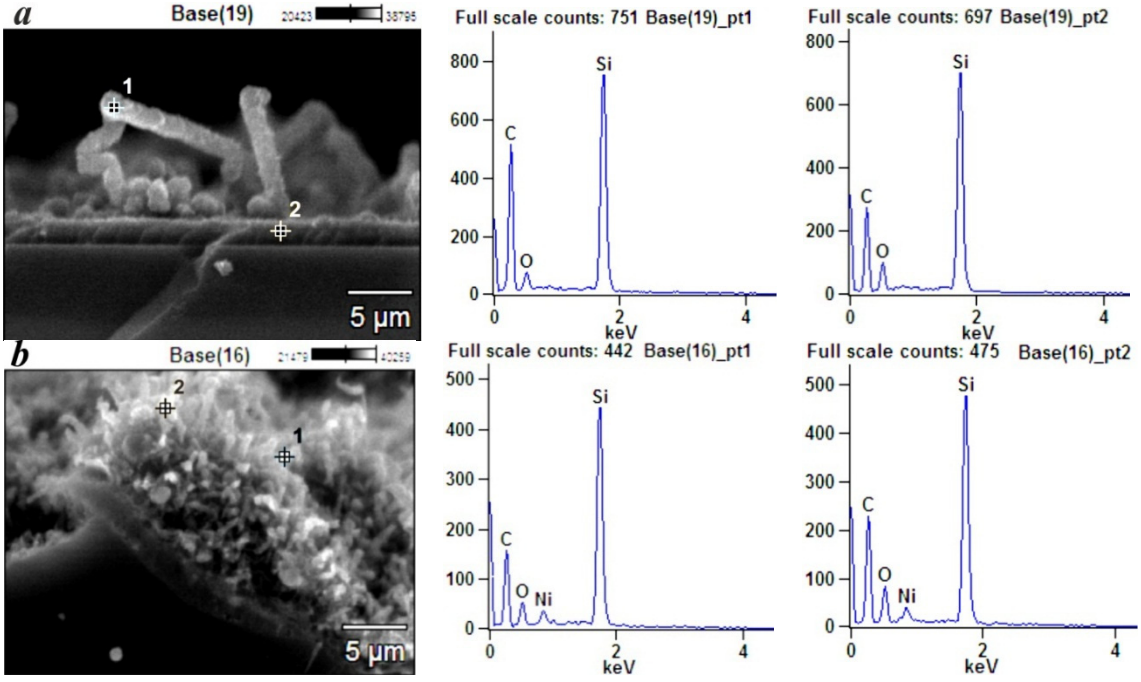

Figure 5 – Energy dispersive X-Ray spectra of samples synthesized at a substrate temperature of 700°C: *a* - Ni/$Si_{(100)}$; *b* - Ni/PS$Si_{(100)}$

The following samples are obtained at a substrate temperature of 800°C. The spectra also contain carbon nanostructures of silicon carbide, *TO* and *LO* groups have shifted to 771.2-788.4 and 928.7-970.1 cm^{-1}. The main carbon peaks *D* and G are observed in the region of 1354.7-1364.4 and 1564.2-1586.4 cm^{-1}. The second-order 2*D* group is located in the region of 2704.6 and 2721.5 cm^{-1}, while *D* + *G* peaks are observed a 2941.6 and at 900.2 cm^{-1}. It can be judged by the intensity of 2*D* and *D* peaks, that samples are rather crystalline.

SEM image (Figure 6*a*) shows that islets of silicon carbide nanostructures are formed in the process of growth. It can be noted that the massive growth of nanostructures occurs on both substrates. Figures 6*b* and 6*d* show that structures formed on polished substrates have a smaller diameter. The energy-dispersive X-Ray spectrum (Figure 7) shows that carbon content in NS for both substrates is ~ 0.6-0.7.

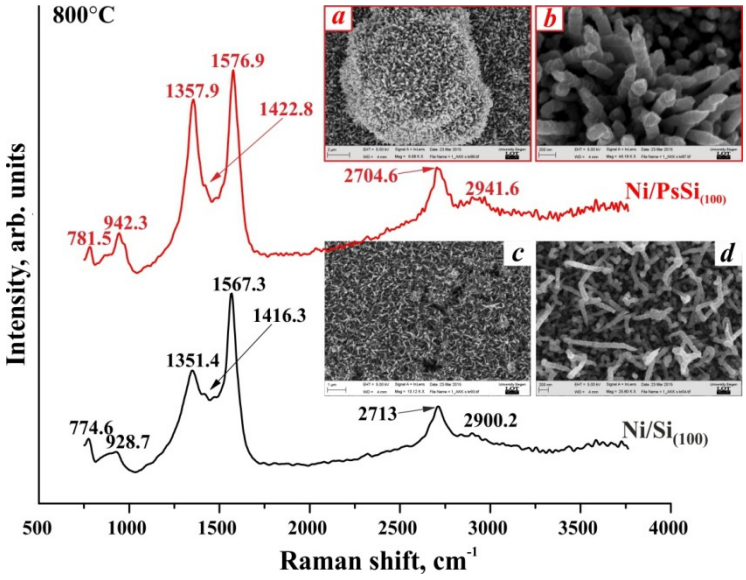

Figure 6 – Raman spectra and SEM images of samples synthesized at a substrate temperature of 800°C: *a, b* - Ni/PSSi$_{(100)}$; *c, d* - Ni/Si$_{(100)}$

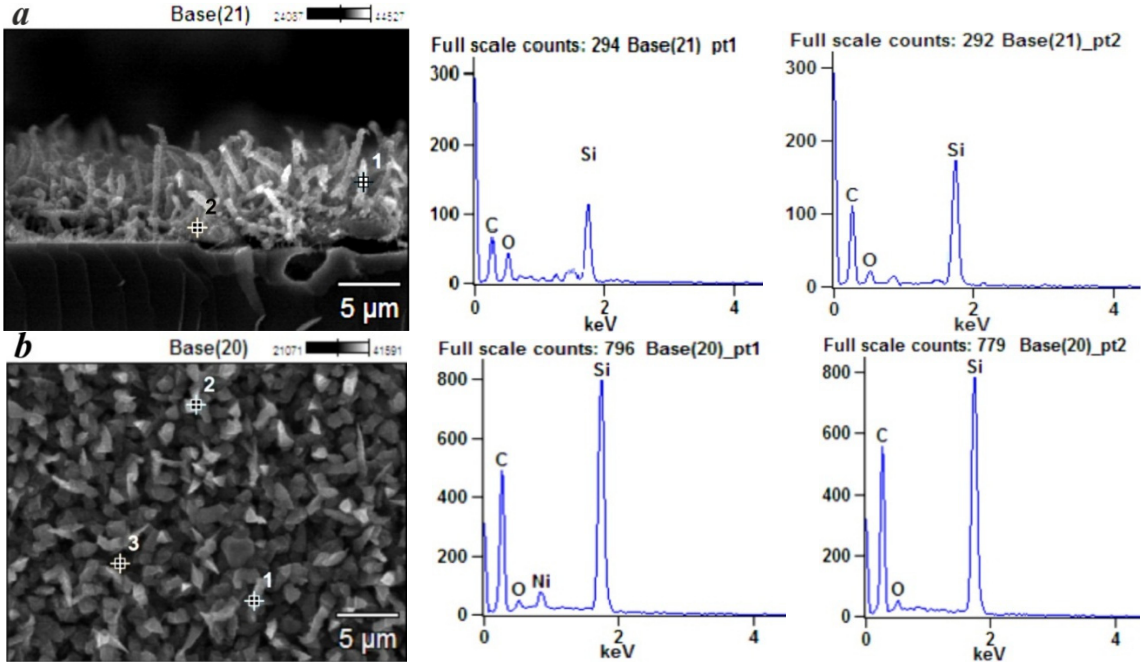

Figure 7 – Energy dispersive X-Ray spectra of samples synthesized at a substrate temperature of 800°C: *a* - Ni/Si$_{(100)}$; *b* - Ni/PSSi$_{(100)}$

As in all samples, shifted silicon carbide peaks are present and the position of the peak of transverse mode has not changed. Peaks within 1426 cm^{-1}, which belong to CH_3 groups [7] can be noted. Peaks *D* and *G* are located in the area of 1348.1-1364.4 and 1580 cm^{-1}. There are groups of the second order 2*D* and *D* + *G* within the limits of 2701.7-2729.9 and 2897.4-2941.6 cm^{-1} on both samples. The second sample contains additional peaks in the region of 2438 and 3252.6 cm^{-1}.

The first peak corresponds to the group *D'*, which is the characteristic group of graphene and allows us to speak about its presence [8]. Whereas, the second one speaks about the presence of C-H bonds in the samples [9].

As can be seen in Figures 8*b* and 8*d*, the formed NS are quite straight and grows oriented, which, presumably, can be influenced by the orientation of the substrate. In addition, it can be seen that NS formed on PS have an average diameter of 200 nm and, as in the previous experiments, a rough surface. The diameter of nanostructures on polished substrates is half as much, as can be seen from Figure 8*d*. It can be noted that growth of NS is massive on both polished Si and PS surfaces. The energy-dispersive X-Ray spectra in Figure 9 indicate that carbon content in NS on both substrates is up to ~ 0.5.

NS synthesized on substrates Ni/PSSi$_{(111)}$ and Ni/Si$_{(111)}$

Figure 10 shows Raman spectra of some samples obtained on nickel films deposited on the surface of polished and porous silicon (111) (Ni/Si$_{(111)}$, Ni/PSSi$_{(111)}$).

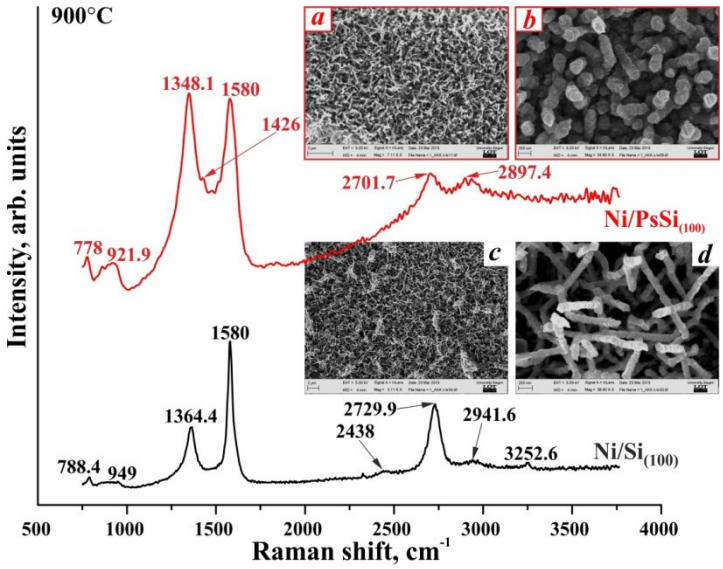

Figure 8 – Raman spectra and SEM images of samples synthesized at a substrate temperature of 900°C: *a, b* - Ni/PSSi$_{(100)}$; *c, d* - Ni/Si$_{(100)}$

Further, spectra of carbon nanostructures obtained at different temperatures on the surface of polished silicon substrates with the orientation [111] were considered. Figure 10*a* shows spectra of nanostructures on polished substrates. The first sample contains the main carbon peaks in the region of 1348.1 and 1596 cm^{-1}. One can note the shift of *G* peak to the high-frequency region ~ 1600 cm^{-1}. In addition to these, displaced silicon carbide groups at 784.9 and 945.7 cm^{-1} can be observed. The peak located within 1416.3 cm^{-1} corresponds to the CH_3 groups [7]. The peak in the region of 2900 cm^{-1} corresponds to 2*D* zone and associated with the boundary point *K* in the Brillouin zone of graphite, which depends on the packing in three-dimensional space. These lines are associated with resonance scattering of light and the participation of two phonons with the same energy but opposite direction of the pulse and give information on the ordering of graphite (graphene) layers [10].

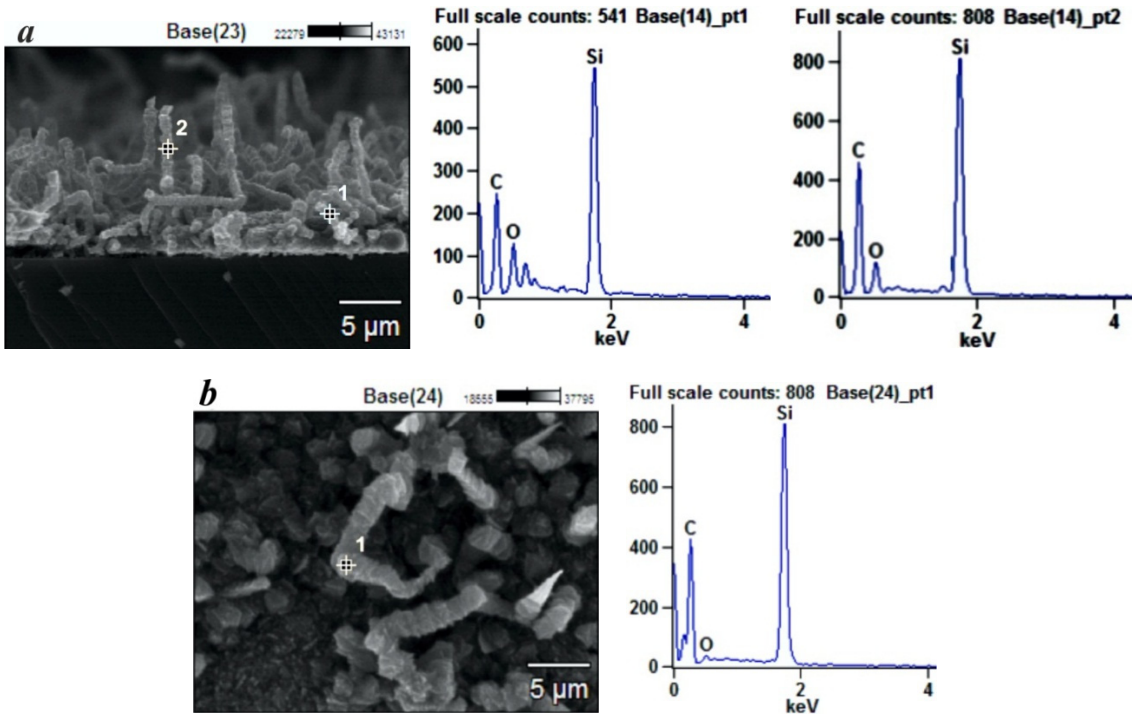

Figure 9 – Energy dispersive X-Ray spectra of samples synthesized at a substrate temperature of 900°C: *a* - Ni/$Si_{(100)}$; *b* - Ni/$PSSi_{(100)}$

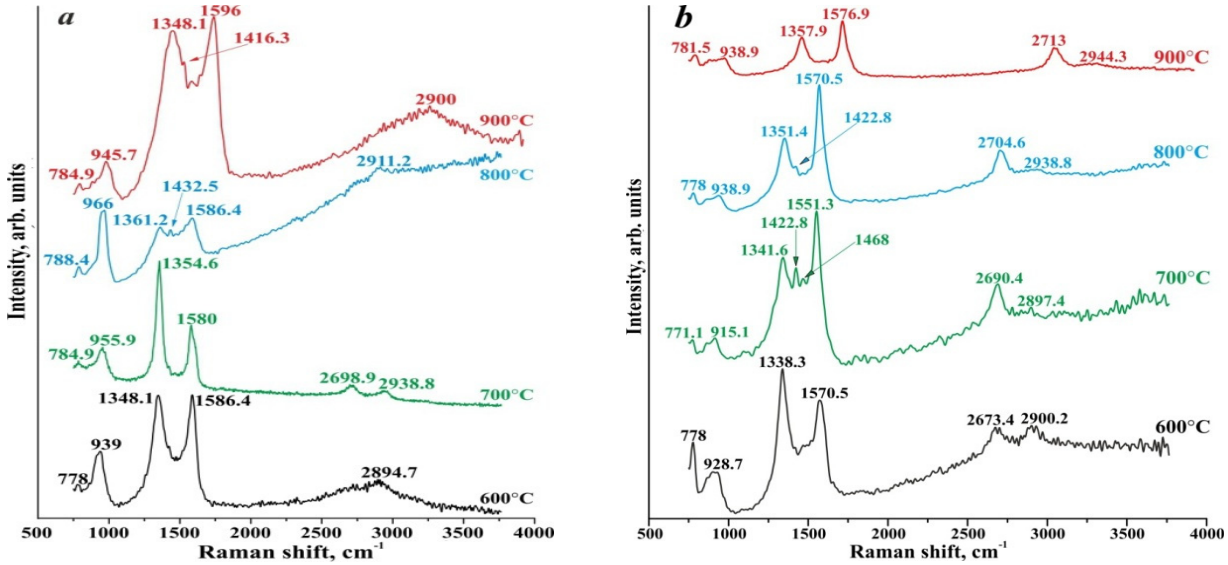

Figure 10 – Raman spectra of samples synthesized on substrates: a – $Ni/Si_{(111)}$, b – $Ni/PSSi_{(111)}$

In the next sample, silicon carbide peaks are not strongly shifted and the most intense than in the remaining samples. One can notice the broadening of the peaks, which may be due to the amorphous structure. The proof of this is the displacement of *D* and *G* peaks to the high-frequency region: 1361.2

and 1586.4 cm^{-1} and the presence of *D* + *G* peak in the region of 2911.2 cm^{-1}. There is also a peak corresponding to CH_3 groups.

There are shifted silicon carbide peaks in the sample obtained at 700°C. But you can see that position of peak of the transverse mode has not changed. *D* and *G* peaks are located in the region of 1348.1 and 1586.4 cm^{-1}. The sample is defective, since the intensity of *D* peak is very high and there is *D* + *G* peak at 2894.7 cm^{-1}.

The main carbon groups "merged" into one peak in the last sample. This can happen because of close location of peaks. There are 3 peaks located at 1367.7, 1442.2 and 1551.3 cm^{-1}, which correspond to the groups *D*, CH_3 and *G*. As in the remaining samples, there are peaks of carbon nanostructures of silicon carbide. *D* + *G* peak is located in the region of 2897.4 cm^{-1}.

In the spectra of Figure 10*b*, peaks of silicon carbide nanostructures are present in the range from 771.1 to 781.5 cm^{-1}. The position of the peak of the transverse mode does not change and lies in the region of 778 cm^{-1} in the samples obtained at 600 and 800°C. The peaks corresponding to the longitudinal mode are observed in the range from 915.1 to 938.9 cm^{-1}. The position of the peak of the longitudinal mode does not change in the first two samples. *D* peak shifts with a decrease in temperature to the low-frequency region, and its intensity also increases. This indicates an increase in the defectiveness of structures. *G* peak is located at 1570.5 cm^{-1} in the samples obtained at 600 and 800°C. It is shifted to the low-frequency region 1551.3 cm^{-1} in a sample synthesized at 700°C, and shifted to the high-frequency region of 1576.9 cm^{-1} in a sample obtained at 900°C. 2*D* peak is observed at 2673.4 - 2713 cm^{-1}. Also there is *D* + *G* peak, which is within the range of 2897.4 - 2944.3 cm^{-1} in all spectra. All obtained carbon nanostructures are carbon nanotubes. Also there are additional peaks at 700 and 800°C in the region of 1422.8 and 1468 cm^{-1}, which appear due to the presence of CH_3 groups [7].

Figure 11 shows results of studies of samples synthesized on nickel films deposited on the surface of polished silicon (111) by SEM.

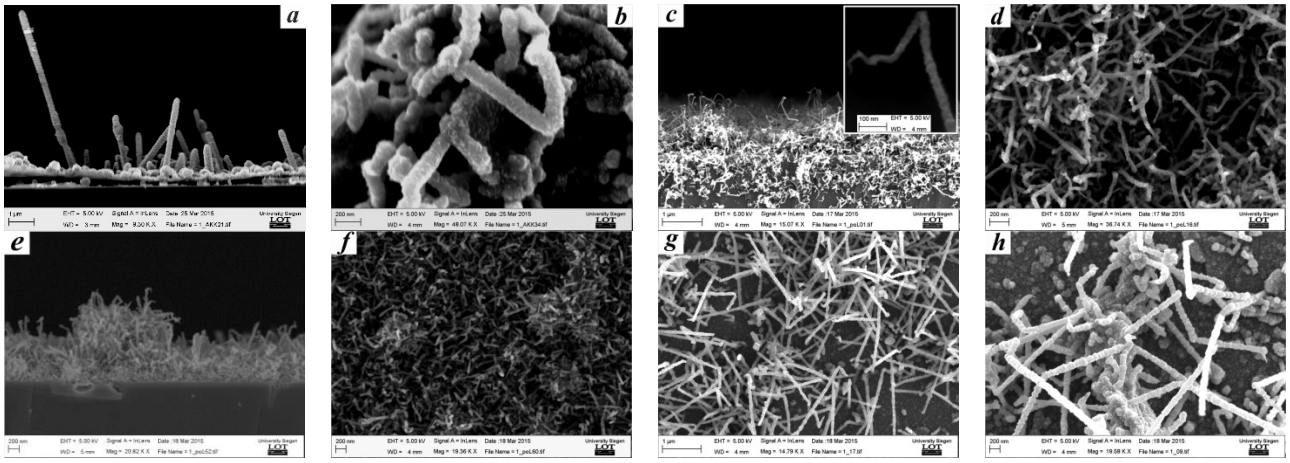

Figure 11 – SEM images of samples synthesized on $Ni/Si_{(111)}$
at different substrate temperatures: *a, b* - 600°C; *c, d* - 700°C; *e, f* - 800°C; *g, h* - 900°C

SEM images of the formed NS show that they have a rough surface. It can be seen that the growth of NS becomes more massive and oriented with increasing temperature. In addition, as can be seen from the figures, the temperature increase also helps to straighten the fibers. It can be seen from Figure 11*g, h* that fibers are curved at a certain angle, which may indicate the influence of the orientation of the substrate on their growth.

Figure 12 shows SEM images of samples synthesized on nickel films deposited on the surface of porous silicon (111).

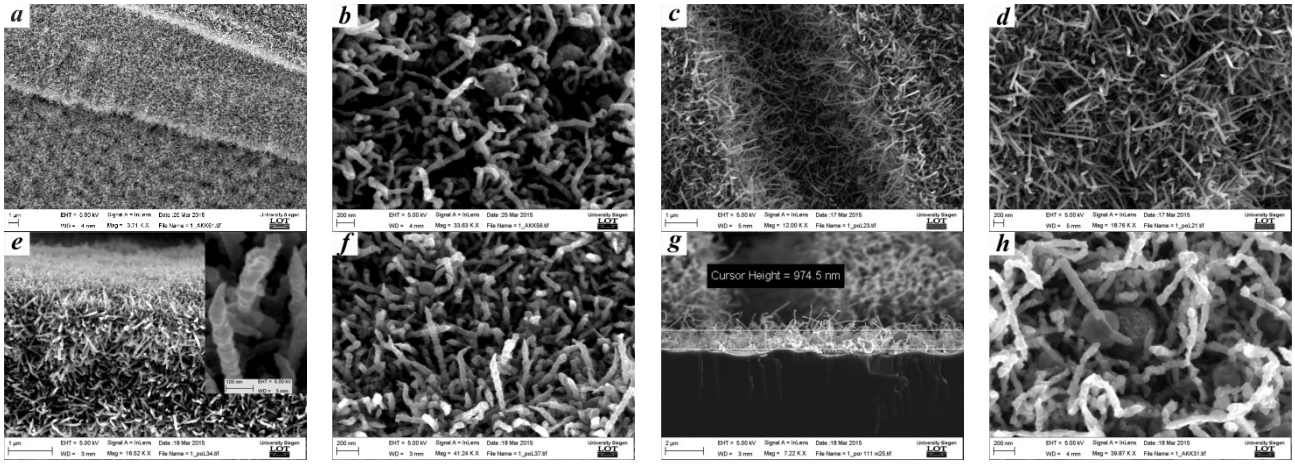

Figure 12 – SEM images of samples synthesized on Ni/PSSi$_{(111)}$
at different substrate temperatures: *a, b* - 600°C; *c, d* - 700°C; *e, f* - 800°C; *g, h* - 900°C

It can be noted that growth of NS on porous silicon substrates is more massive in comparison with polished substrates. The samples obtained at 700°C grow in oriented manner and are quite straight. In comparison with Figure 11, the dependence of NS growth on temperature is not traced in this series of experiments. Figure 12*g* show that the height of synthesized NS is 974.5 nm. According to figures 11*c* and 12*e*, the obtained structures have a diameter of ~ 100 nm.

Conclusion

Experiments on synthesis of SiC and C nanostructures on Ni buffer layer by the method of microwave plasma assisted chemical vapor deposition were carried out.

Studies by scanning electron microscopy have shown that the formed nanostructures have a diameter of 100-170 nm and a rough surface. Analysis of results of scanning electron microscopy of samples shows that the growth of nanostructures on the surface of porous silicon is more massive than on polished Si. Energy dispersive X-Ray spectra indicate that carbon content in NS varies from ~ 40 to ~ 80%.

The results of studies by Raman scattering confirmed that there are carbon nanostructures of silicon carbide with 3C-SiC polytype structure. It was determined that the most optimal temperature for obtaining nanostructures is 800°C. It is also possible to note the presence of the main carbon peaks in the range of ~1300 and ~1500 cm^{-1}, which correspond to carbon nanostructures on both types of substrates.

For a more detailed analysis of the structure of the produced NS, it is necessary to conduct additional studies using transmission electron microscopy and diffraction of electrons, as well as X-Ray diffraction analysis.

Acknowledgment

The authors thank c.p.-m.s. Dikhanbaev Kadyrzhan for help in preparing samples of porous silicon, as well as c.p.-m.s. Mansurova Madina for the discussion and proofreading of the text of the article.

The work was carried out with partial financial support of the grants of Science Committee of the Ministry of Education and Science of the Republic of Kazakhstan No. 3823/ГФ4, and No. 3816/ГФ4.

References

[1] E. W. Wong, P. E. Sheehan, C. M. Lieber. Nanobeam Mechanics: Elasticity. Strength. and Toughness of Nanorods and Nanotubes // Science. – 1997. – Vol. 277**.** – P. 1971-1975.

[2] Z. S. Wu, S.Z. Deng, N.S. Xu, J. Chen, J. Zhou. Needle-shaped silicon carbide nanowires: Synthesis and field electron emission properties //Appl. Phys.Lett. – 2002. – Vol. 80. – P. 3829.

[3] G.V. Berezhkova. Filament like crystals. Moscow: Nauka. – 1969. – 159 p (in Russian).

[4] A. Chrysanthou, P. Grieveson. Synthesis of SiC from rice husks catalysed by iron. cobalt or nickel // J. Mater. Sci. – 1991. – Vol. 26. – P. 3463-3476.

[5] V.L. Kuznetsov, A.N. Usoltseva, I.N. Mazov. General regularities of the formation of carbon nanostructures and filamentary crystals of silicon carbide on the surface of metallic catalysts. Russ. Chem. J. – 2004. – Vol. XLVIII. – No. 5. – P. 37-45 (in Russian).

[6] D. Wang, C. Xue, H. Bai, N. Jiang. Silicon carbide nanowires grown on graphene sheets //Ceramics International. Access mode: http://dx.doi.org/10.1016/j.cer amint.2014.12.117.

[7] K.B. Dillon, D.W.H. Rankin. Spectroscopic Properties of Inorganic and Organometallic Compounds // Royal Society of Chemistry. – 2000. – Vol. 33. – P. 311.

[8] Ya.B. Volkova, E.V. Rezchikova, V.A. Shakhnov. Methods of obtaining and results of the study of the properties of grapheme // Engineering Journal: Science and Innovation. – 2013. – Vol. 6.

[9] I. Rehman, Z. Movasaghi, Sh. Rehman. Vibrational Spectroscopy for Tissue Analysis. – P. 281.

[10] A.C. Ferrari. Raman spectroscopy of graphene and graphite: Disorder. electron-phonon coupling. doping and nonadiabatic effects // Solid State Communications. – 2007. – V.143. – P. 47-57.

UDC 669.018; 621.315.392

The percolation mechanism of conductivity in nanocomposite a-C:H<Ag+Ti> films

[1*]Mukhametkarimov Ye.S., [1]Mikhailova S.L., [1]Dautkhan K., [1]Bashen A., [1]Zhumatayev Zh. N., [2]Rofman O.V., [1]Maksimova S.Ya., [1]Prikhodko O.Yu.[1]

[1]Open Type National Nanotechnological Laboratory
al-Farabi Kazakh National University, Almaty, 050040 Kazakhstan
[2]National University of Science and Technology, MISiS, Russia
**e-mail: ye.mukhametkarimov@gmail.com*

The presented work is about percolation mechanism of electrical conductivity of composite a-C:H<Ag+Ti> films. The a-C:H<Ag+Ti> thin films were deposited onto quartz substrates by ion-plasma magnetron sputtering of a combined target. Resistance of the produced films has been measured using «two probe» method to obtain concentration dependence of electrical conductivity. Conductivity of a-C:H<Ag+Ti> films was described theoretically in two ways: using the classical theory of percolation and a general effective medium (GEM) theory. Staircase percolation can be seen from the experimental results. The first percolation threshold occurs at the concentration $x_c = 0.015$ and the second one - at $x_c = 0.07$. This could take place due to the fact that a-C:H<Ag+Ti> composite material consist of two different inclusions, silver and titanium dioxide nanoparticles. The percolation mechanism of a-C:H<Ag+Ti> film conductivity could be described by classical percolation theory and by effective medium model as well.

Key word: Amorphous carbon thin films, silver nanoparticles, nanocomposite, percolation, effective medium theory.
PACS:61.00

Introduction

Composite materials based on the dielectric matrix with metal nanoparticles inclusions are of considerable interest in connection with possibility of their wide practical application in various fields of science and technology. A wide variety of functional properties of these composites allows using them, starting from energy sector (in solar cells) to targeted delivery of drugs in medicine [1-5].

Plasmon resonance absorption of electromagnetic radiation in the visible region of the spectrum on free surface electrons of metal nanoparticles takes place in nanocomposite materials based on the dielectric or semiconductor high-resistivity matrix and some metals nanoparticles in it [6]. Role of the matrix in such nanocomposite materials is to isolate the metal nanoparticles and preventing their agglomeration. Parameters of the resonance absorption are determined by dielectric permittivity of the matrix and by physical and chemical nature of the metal [6,8]. This is shown in the studies of composite materials based on semiconductor matrices as SnO_2 [9], ZnO [10] and CdS [11, 12] and polymer matrices [13] with inclusions of silver and gold nanoparticles.

It is significant, that in such composite materials, under certain conditions, great surface amplification of Raman scattering of light (SERS effect) [14] is manifested, which allows to detect even individual molecules, and using silver nanoparticles, significantly enhance the antibacterial properties of coatings as well.

In modern nanomaterials science, amorphous diamond-like hydrogenated carbon films (a-C:H) have a special interest of researchers. This is due to a number of unique mechanical and electronic properties of these films. Taking into account high mechanical strength and reliability of the films, electronic devices made on the basis of these materials have extremely high speed, power, able to operate in a very wide temperature range and have high radiation resistance.

Diamond-like carbon materials containing metal nanoparticles represent a new class of nanostructured materials, called nanocomposites. In

connection with this, development of nanomaterials with new properties based on diamond-like carbon media modified by metal impurities that significantly differ in nature by chemical interaction with carbon atoms and study of their structure and electronic properties is one of the most relevant and extremely important areas of research in nanotechnology and nanomaterial science [15].

In addition, to optical effects of the a-C:H<Ag+Ti> film [16], there are unique electrical properties. In the a-C:H<Ag+Ti> films, a double percolation transition with respect to conductivity is realized. Films with concentration of silver nanoparticles near the percolation threshold can be promising for creating highly sensitive small bending sensors [17, 18].

Experiment.

Deposition of a-C:H<Ag+Ti> nanocomposite films was carried out in the vacuum chamber using ion-plasma magnetron sputtering of the combined target. Basic technological parameters of a-C:H <Ag+Ti> film production represented in the Table 1.

Table 1 – Basic technological parameters for a-C:H <Ag+Ti> film production

Working gas composition	The pressure in chamber P, Pa	Deposition temperature, ^{o}C	The distance from the target to the substrate, cm	Specific discharge power, W/cm	The magnetic field strength H, mlT
96% Ar + 4% CH_4	0.8-1.0	100	3.5	3-4	~30

High purity argon (Ar) and methane (CH_4) gases mixture and combined target of polycrystalline graphite with the purity of 99.99%, silver (99.99%) and titanium (99.99%) were used to produce a-C:H<Ag+Ti> films. The a-C:H<Ag+Ti> films were deposited on a glass and quartz substrates.

Resistance of the produced films has been measured using «two probe» method to determine concentration dependence of electrical conductivity which represented on Figure 2. Note that conductivity of a-C:H<Ag+Ti> films at the maximum of Ag concentration remains much lower with respect to conductivity of polycrystalline graphite. This means that in these films there is no through-conduction channel over the regions of graphite-like carbon with sp^2-hybridized bonds presented in diamond-like matrix with sp^3-hybridized bonds.

Simulation of the percolation conductivity processes in a-C:H<Ag+Ti> nanocomposite films

Conductivity of nanocomposite material can be described in two ways: using the classical theory of percolation (flow) and the model of a general effective medium.

Let us consider the main conclusions of percolation theory for conductivity analysis of the disordered structure, which is a set of conducting elements with concentration x and conductivity σ_M randomly distributed in a dielectric matrix with conductivity σ_D ($\sigma_D << \sigma_M$). According to percolation theory, conducting structure is a set of percolation clusters. For small values σ_M of x, all clusters are small. However, as we reach the percolation threshold, individual clusters merge, and their average size increases. At a certain concentration of x_c, the percolation cluster becomes infinite, i.e. there appears a path connecting remote to arbitrarily large distances the conducting regions inside the dielectric matrix and wholly passing through the conducting phase.

To the left of the percolation threshold x_c, at a sufficiently large distance from it, the total conductivity of the medium can be represented by [19]

$$\sigma_c = \sigma_D (x_{cr} - x)^{-q}, \text{ for } x < x_c, \qquad (1)$$

where σ_D is conductivity of the matrix.

To the right of the percolation threshold, the concentration dependence of conductivity varies according to the law

$$\sigma_c = \sigma_M (x - x_{cr})^{t}, \text{ for } x > x_c, \qquad (2)$$

where σ_M is the conductivity of the conducting phase.

Conductivity at the point of appearance of the infinite percolation cluster is described by

$$\sigma(x_c) = \sigma_M \left(\frac{\sigma_D}{\sigma_M} \right)^{s}, \; x = x_c, \; s > 0. \qquad (3)$$

The quantities q, t and s in (1-3) are called the critical indices of the conducting cluster.

The curve of theoretical dependence $\sigma(x)$ describing $\sigma(x)$ before and after the percolation threshold is shown in Figure 1. The transition curve (1) to (2) takes place in a small interval Δ in the vicinity of the x_c point. Relation (1) is satisfied if $\sigma(x) << \sigma(x_c)$ or $x_c - x >> \Delta$, and relation (2) holds for $\sigma(x_c)<<\sigma(x)<<\sigma(x_M)$ or $x - x_c>> \Delta$. The conducting cluster is also characterized by a correlation radius or a characteristic size l

$$l = l_o \left|\frac{x-x_c}{x_c}\right|^{-\nu}, \quad (4)$$

where ν is critical index, also called the critical index of the correlation radius, l_o is the lattice period.

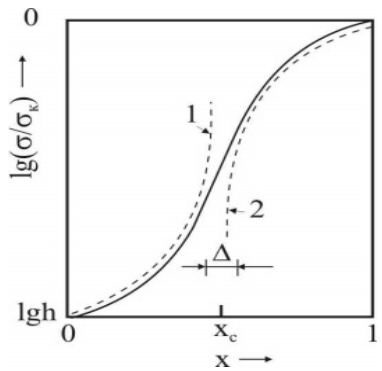

1 - $\sigma(x)$ at $x < x_c$, 2 - $\sigma(x)$ at $x > x_c$.

Figure 1– The theoretical dependence σ(x) (solid line) [19]

Quantity l for $x < x_c$ is in the order of cluster size itself, and for $x > x_c$ in the order of nonconducting pores size in it.

The critical indices of the percolation theory q, t, s and ν are related to each other by the relations

$$q = \frac{t}{s} - t, \quad (5)$$

$$t = 1 + \nu(d-2), \quad (6)$$

where d is dimension of space. For a three-dimensional composite the classical values are: t = (1.6 ÷ 2.0), q≈1, s≈0.62.

We note that index t plays a very important role, since, unlike the percolation threshold x_c, it does not depend on the type of the problem, but depends only on the dimensionality of the space. Therefore, in real systems, this index is primarily compared with the theory. On the other hand, the universality of critical indices of percolation theory just allows us to involve it for the analysis of heterogeneous disordered structures conductivity.

Figure 2 shows concentric dependence of conductivity of a-C:H <Ag+1.0 at.% Ti> films. In this figure, silver concentration x is represented as the volume fraction in the matrix of the films. The curves describing behavior of concentration dependence of conductivity up to (curves 1 and 2) and after (percolation curves 1 'and 2') are represented using expressions (1) and (2). It follows from this approach that concentration dependence experimental data of a-C:H<Ag+1.0 at.% Ti> films conductivity can be described by two percolation transitions (the so-called staicase percolation).

Note that there are inclusions of both Ag and TiO_2 nanoparticles in the matrix of the studied a-C:H<Ag+Ti> films, and several percolation transitions can occur in such nanocomposites.

Let us consider the concentration dependence of the a-C:H<Ag+Ti> films conductivity using the effective-medium model (General Effective Medium, GEM), which is used to describe concentration dependences of conductivity of composite materials [20]. The expression to determine the conductivity σ in the theory of general effective medium is written as follows [20]

$$\frac{x(\sigma_D^{\frac{1}{t}} - \sigma(x)^{\frac{1}{t}})}{\sigma_D^{\frac{1}{t}} + A\sigma(x)^{\frac{1}{t}}} = \frac{(1-x)(\sigma_M^{\frac{1}{t}} - \sigma(x)^{\frac{1}{t}})}{\sigma_M^{\frac{1}{t}} + A\sigma(x)^{\frac{1}{t}}} = 0, \quad (7)$$

$$A = \frac{1-x_c}{x_c}, \quad (8)$$

where the exponent is defined as $t = (1 - x_c)/(1 - l)$.

The results of a comparison of theoretical description of the percolation process according to the classical theory and general effective medium model with experimental values of concentration dependence of conductivity of a-C:H<Ag+1.0 at.% Ti> films are shown in Figure 2, curve 3.

From the figure 2 it follows that classical theory of percolation and approach based on the general effective medium model make it possible to describe the region of percolation transition before and after the percolation threshold in a-C:H<Ag+1.0 at.% Ti> nanocomposite films.

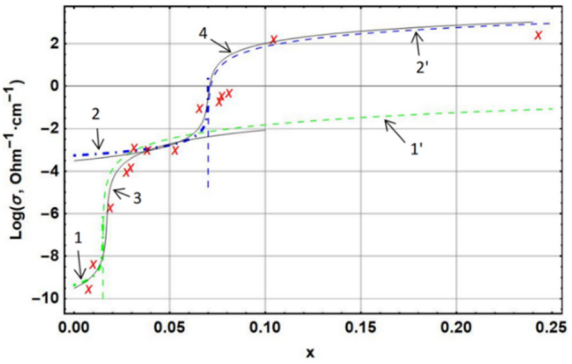

X: are the experimental values
1: $x_c = 0.015$, $t = 1.7$; 1': $x_c = 0.07$, $t = 1.4$;
2: $x_c = 0.015$, $q = 0.9$; 2': $x_c = 0.07$, $q = 0.9$;
3 и 4 - effective environment model with parameters $x_c = 0.018$, $t = 1$, $\sigma_D \approx 3 \cdot 10^{-10}\ Ohm^{-1} \cdot cm^{-1}$, $\sigma_M \approx 0.5\ Ohm^{-1} \cdot cm^{-1}$, $l = 0.4$.

Figure 2 - Theoretical (1 and 1 ', 2 and 2', 3 and 3 ') and experimental (x) dependence of conductivity of a-C:H<Ag+1.0 at.% Ti> nanocomposite films on Ag volume fraction

Conclusion

Conductivity of a-C:H<Ag+Ti> films at the maximum of Ag concentration remains much lower compared to conductivity of polycrystalline graphite. This means that in these films there is no through-conduction channel over the regions of graphite-like carbon with sp^2-hybridized bonds presented in diamond-like matrix with sp^3-hybridized bonds. From concentration dependence of conductivity we conclude that two percolation transition occur in the obtained a-C:H<Ag+Ti> composite material. These percolation mechanisms of film conductivity could be adequately described by the classical percolation and general effective medium theories.

Acknowledgment

This research was supported by grant 4608/GF4 of the Committee of Science of the Ministry of Education and Science of the Republic of Kazakhstan.

Reference

1. H. Wenbo, P. Pavaskar, L. Zuwei, J. Theiss, M. Aykol, B. Stephen. Plasmon resonance enhancement of dye sensitized solar cells // Energy Environ. Sci. –2011. – Vol.4. –P.4650–4655.

2. H.A. Atwater, A. Polman. Plasmonics for improved photovoltaic devices // Nature Materials. – 2010. – Vol.9. – P. 205-213.

3. N. Jeffrey, W. Anker, P. Hall, O. Lyandres, N. C. Shah, Jing Zhao, R. P. Van Duyne. Biosensing with plasmonic nanosensors // Nature Materials. 2008.–Vol. 7. – P. 442-453.

4. K. Prashant, Jain. Xiaohua Huang, H. Ivan, H. El-Sayed, M. A. El-Sayed. Noble Metals on the Nanoscale: Optical and Photothermal Properties and Some Applications in Imaging. Sensing. Biology and Medicine // Accounts Of Chemical Research. – 2008. –Vol. 41. – P.1578-1586.

5. Jiongxin Lu, C. P. Wong. Recent Advances in High-k Nanocomposite Materials for Embedded Capacitor Applications // IEEE Transactions on Dielectrics and Electrical Insulation. – 2008. – Vol. 15. – P. 1322.

6. M. Quinten. Optical Properties of Nanoparticle Systems // Wiley-VCH. Verlag GmbH & Co. KGaA, Weinheim. Germany – 2011. – P. 502.

7. A. M. Mahmoud, Maysamreza Chamanzar, Ali Adibi, Mostafa A. El-Sayed. Effect of the Dielectric Constant of the Surrounding Medium and the Substrate on the Surface Plasmon Resonance Spectrum and Sensitivity Factors of Highly Symmetric Systems: Silver Nanocubes // J. Am. Chem. Soc. 2012. – Vol. 134. – P.6434–6442.

8. E. Hutter, J. H. Fendler. Exploitation of Localaized Surface Plasmon Resonance // Adv. Mater. – 2004. – Vol. 16. –P.1685.

9. W. Wu, L. Liao, S.F. Zhang, J. Zhou, X.H. Xiao, F. Ren, L.L. Sun, Z.G. Dai, C.Z. Jiang. Non-centrosymmetric Au/SnO_2 Hybrid Nanostructures with Strong Localization of Plasmonic for Enhanced Photocatalysis Application // Nanoscale. – 2013. – Vol.5. – P.5628.

10. Y.K. Mishra, V.S.K. Chakravadhanula, V. Hrkac, S. Jebril, D.C. Agarwal, S. Mohapatra, D.K. Avasthi, L. Kienle, R. Adelung. Crystal growth behaviour in Au-ZnO nanocomposite under different annealing environments and photoswitchability // J. Appl. Phys. – 2012. – Vol. 112. – P.064308.

11. H. DuanaYimin Xuan. Synthesis and optical absorption of Ag/CdS core/shell plasmonic nanostructure // Solar Energy Materials and Solar Cells. -2014. – Vol.121. –P. 8-13.

12. D. Ziemannn, V. May. Exciton Formation and Quenching in a Au/CdS Core/Shell Nanostructure // J. Phys. Chem. Lett. – 2015. – Vol.6. – P.4054–4060.

13. Long-De Wang, Tong Zhang, Xiao-Yang Zhang, Yuan-Jun Song, Ruo-Zhou Li, Sheng-Qing Zhu. Optical

properties of Ag nanoparticle-polymer composite film based on two-dimensional Au nanoparticle array film // Nanoscale Res. Lett. –2014. Vol.9. – P. 155.

14. B. Sharma, R. F. Renee, A-I Henry, E Ringe, P. Richard, Van Duyne. SERS: Materials. applications. and the future // Materials Today. – 2012. – Vol.15. – P. 16-25.

15. O. Yu. Prikhodko, S. L. Mikhailova, E. C. Muhametkarimov, S. Ya. Maksimova, N. K. Manabaev, K. Dauthan. Optical properties of a-C:H thin films modified by Ti and Ag /Proc. of SPIE. Nanostructed Thin Films IX. San-Diego. California. USA. – 2016. – Vol. 9929. – P. 99291G-1 – 9929G-6.

16. O.Yu. Prikhodko, Ye.S. Mukhametkarimov, S.L. Mikhailova, K. Dauthan, S.Ya. Maksimova. Structure and Phase Composition of Thin a-C:H Films Modified by Ag and Ti // Optics and Spectroscopy. –2017. – Vol. 123. – P.353–358.

17. M. O. Mendoza, M. Edna, A. Valenzuela, E. Prokhorov, G. Luna-Barcenas, S. Kumar-Krishnan. Percolation phenomena in polymer nanocomposites // Adv. Mater. Lett. – 2016. – Vol. 7. –P. 353-359.

18. M. Segev-Bar, H. Haick. Flexible Sensors Based on Nanoparticles // ASC Nano. – 2013. –Vol. 7. –P. 8366-8378.

19. A.L. Efros, B.I. Shklovskii. Critical Behavior of Conductivity and Dielectric Constant near the Metal-Non Metal Transition Threshold// Phys. Stat. Sol. B. – 1976. – Vol. 76. – P. 475-485.

20. I. Balberg. The percolation staircase model and its manifestation in composite materials // The European Physical Journal B. – 2013. – Vol. 86. – P. 1-17.